

1 **Ocean Circulation Connecting Fram Strait to Glaciers off North-East**

2 **Greenland: Mean Flows, Topographic Rossby Waves, and their Forcing**

3 Andreas Münchow*

4 *University of Delaware, Newark, Delaware*

5 Janin Schaffer

6 *Alfred Wegener Institute, Bremerhaven, Germany*

7 Torsten Kanzow

8 *Alfred Wegener Institute, Bremerhaven, Germany*

9 *Corresponding author address: Andreas Münchow, College of Earth, Ocean, and Environment,

10 University of Delaware, Newark, DE 19716.

11 E-mail: muenchow@udel.edu

ABSTRACT

12 From 2014 through 2016 we instrumented ~ 80 km wide Norske Trough
13 near 78° N latitude that cuts across the 250 km wide shelf from Fram Strait
14 to the coast. Our measurements resolve a ~ 10 km wide bottom-intensified
15 jet that carries 0.27 ± 0.06 Sv of warm Atlantic water from Fram Strait to-
16 wards the glaciers off North-East Greenland. Mean shoreward flows along
17 the steep canyon walls reach 0.1 ms^{-1} about 50 m above the bottom in 400
18 m deep water. The same bottom-intensified vertical structure emerges as the
19 first dominant empirical orthogonal function that explains about 70-80% of
20 the variance at individual mooring locations. We interpret the current vari-
21 ability as remotely forced wave motions that arrive at our sensor array with
22 periodicities longer than 6 days. Coherent motions with a period near 20 days
23 emerge in our array as a dispersive topographic Rossby wave that propagates
24 its energy along the sloping canyon towards the coast with a group speed of
25 about 63 km per day. Amplitudes of wave currents reach 0.1 ms^{-1} in the
26 winter of 2015/16. The wave is likely generated by Ekman pumping over the
27 shelfbreak where sea ice is always mobile. More than 40% of the along-slope
28 ocean current variance near the bottom of the canyon correlates with verti-
29 cal Ekman pumping velocities 180 km away. In contrast the impact of local
30 winds on the observed current fluctuations are negligible. Dynamics appear
31 linear and Rossby wave motions merely modulate the mean flow.

32 1. Introduction

33 Warm Atlantic waters accelerate the melting of Greenland glaciers (Holland et al. 2008; Straneo
34 and Heimbach 2013; Johnson et al. 2011; Mayer et al. 2018). While the details of ocean melting
35 vary from glacier to glacier (Jackson et al. 2014; Carroll et al. 2016; Washam et al. 2019), ocean
36 processes contribute to retreating glaciers as heat is advected across continental shelves (Suther-
37 land et al. 2014; Inall et al. 2014; Jackson et al. 2014). We currently do not know how the heat
38 from the deep Atlantic Ocean crosses shallow continental shelves to reach Greenland's coastal
39 glaciers. Presenting new observations from North-East Greenland, we demonstrate that subsur-
40 face jets over sloping bottom topography advect heat through canyons towards marine terminating
41 glaciers in North-East Greenland such as Nioghalvfjærdsbræ (Mayer et al. 2000; Schaffer et al.
42 2017) and Zachariæ Isstrøm (Mouginot et al. 2015).

43 Submarine canyons often enlarge across-shelf exchange of mass, buoyancy, and vorticity at both
44 polar (Münchow and Carmack 1997) and mid-latitudes (Freeland and Denman 1982). A cyclonic
45 flow over a canyon on the shelf off Vancouver Island, Canada, for example, caused high algae
46 blooms near the surface due to a convergence of the near-bottom frictional Ekman layer and at-
47 tendant upwelling of nutrient-rich waters into the upper layer (Freeland and Denman 1982). Allen
48 (1996) and Allen and Hickey (2010) simulated the physics of canyon upwelling while Hickey and
49 Banas (2008) explained high productivity off the northern US-Canadian West Coast by interactions
50 of the wind-driven California Current, buoyancy-driven Strait of Juan de Fuca outflow, and canyon
51 dynamics. Coastal Greenland, too, features wind- and freshwater-driven currents (Sutherland and
52 Pickart 2008; Münchow 2016; Håvik et al. 2017) along with prominent canyon systems (Arndt
53 et al. 2015) that amplify across-shelf exchanges (Sutherland and Cenedese 2009). Off North-

54 East Greenland such exchange moves subsurface warm offshore water towards coastal glaciers via
55 Norske Trough (Schaffer et al. 2017) which cuts across a broad continental shelf.

56 Bourke et al. (1987) first described surveys of the continental shelf off North-East Greenland in
57 1979 and 1984 from coastal glaciers to Fram Strait near 79° N latitude. Belgica Bank emerged
58 as a shallow submarine shoal between 78-80° N latitude, Norske Trough as a 400 m deep canyon
59 to the south and west of Belgica Bank (Fig. 1). Wadhams et al. (2006) noted that the 20-80
60 km wide canyons were poorly mapped. Nevertheless, early investigators defined water masses,
61 estimated geostrophic velocities (Bourke et al. 1987), and suggested northward flow along the
62 coast (Schneider and Budéus 1995). Shelf waters near 79° N latitude differed from those found
63 farther south near 77° N latitude which led Budéus et al. (1997) to concluded that "... *there is no*
64 *one-directional through-flow of deeper waters in the trough system ...*". More recent studies such
65 as Richter et al. (2018) provide synoptic velocity observations that describe a largely barotropic
66 Arctic outflow north of 79° N which transforms into a more baroclinic boundary current near the
67 shelfbreak off North-East Greenland that flows south past Denmark Strait as the East Greenland
68 Current (Håvik et al. 2017).

69 The first direct ocean current measurements from the shelf and canyon systems of North-East
70 Greenland were reported by Johnson and Niebauer (1995) and Topp and Johnson (1997) during a
71 1992/93 experiment. Two moorings near 80° N (Topp and Johnson 1997) and survey data sketched
72 out a clockwise circulation around Belgica Bank. These early measurements did not always re-
73 solved the internal Rossby radius $R_i \sim 10$ km which scales stratified flows on a rotating earth (Gill
74 1982). This scale is similar to the width of sloping topography which is small relative to the 80-
75 km wide canyon. Our 2014-16 mooring and survey data resolve ocean currents at this scale across
76 both slopes of the wide canyon.

77 Sea ice always covers the ocean off North-East Greenland (Reeh et al. 2001). During the 20th
78 century the continental shelf featured large areas of fast-ice throughout the year (Hughes et al.
79 2011). The general clockwise circulation around Belgica Bank (Budéus and Schneider 1995)
80 under the fast-ice then created a polynya to the north of the fast-ice whose biological productivity
81 functioned as a carbon sink (Yager et al. 1995). More recently, satellite imagery shows that this
82 landfast ice breaks up for about two months in summer of the 21st century (Sneed and Hamilton
83 2016). Our observations from 2014 through 2016 thus describe ocean currents during both summer
84 and winter seasons when the coastal sea ice is mobile and landfast, respectively.

85 We use a diverse set of data to describe how ocean currents, temperature, sea ice, and winds
86 are distributed in time and space on the vast continental shelf off North-East Greenland. Ocean
87 current moorings across Norske Trough form the focus of our study that was designed to quantify
88 dominant vertical and horizontal scales. These scales relate to dynamics that must be resolved
89 to adequately describe across-shelf exchange of heat and buoyancy. We quantify the hypothesis
90 that topographic Rossby waves contribute to the temporal variability of bottom-intensified currents
91 (Rhines 1970; Pickart and Watts 1990) and that a spatially variable wind field over the slope of
92 Fram Strait generates such waves with 20 day periods. Alternative generation mechanism exist
93 and we speculate about spatially coherent oscillations with periods of 6 and 11 days.

94 **2. Study area, Data, and Methods**

95 Norske Trough connects deep Fram Strait in the east to coastal glaciers in the west. The trough
96 starts as broad topographic depression near longitude 10° W, narrows to 80 km near Isle de France
97 at latitude 77° N, and narrows farther to 30 km adjacent to a chain of islands (Fig. 1). The canyon
98 cuts across the 300 km wide continental shelf (Arndt et al. 2015).

99 In June 2014 we deployed seven moorings to measure ocean currents and water properties in
 100 Norske Trough which serves as a potential pathway from the deep ocean to coastal glaciers off
 101 North-East Greenland such as Nioghalvfjærdsbræ and Zachariæ Isstrøm (Fig. 1). We recovered
 102 all instruments more than 2 years later in August 2016 (Table 1). Each mooring included 75 kHz
 103 Acoustic Doppler current profilers (ADCP) of Teledyne RD Instruments.

104 We employed two distinct mooring designs (Table 1): Two ADCPs contain batteries inside the
 105 pressure housing that also contains electronics and transducer assemblies (Design-A). The two
 106 ADCPs were mounted inside a cage shackled to a standard mooring line containing additional
 107 instruments. The ADCP can pitch, roll, and swivel on the mooring line. Tilt sensor measure these
 108 mooring motions. In contrast, five ADCPs have their transducers placed 3-m above the bottom
 109 atop a flat steel buoy (Design-B). External battery cases, acoustic releases, SeaBird SBE37sm
 110 Microcats, and additional steel buoys are all mounted within a single stiff frame that can pitch
 111 and roll, but not swivel (Münchow and Melling 2008). No additional mooring lines or sensors
 112 are above the ADCP transducer heads. The torsionally rigid design minimizes compass errors,
 113 if one knows the fixed orientation of the instrument on the sea floor. Appendix-A describes data
 114 processing details to move data from both mooring designs into a common earth-referenced co-
 115 ordinate system.

116 Bottom-mounted ADCP depend on scatterers in the water column to reflect sound back to the
 117 transducers to estimate the Doppler shift in the transmit frequency $F_0 = 75 \text{ kHz}$ in vertical bins $D =$
 118 8 m . Our broadband ADCPs use two encoded pulses with an ambiguity velocity $V_a = 1.75 \text{ m s}^{-1}$
 119 and beam angle $\theta = 30 \text{ deg}$. Random single-ping velocity errors thus are (RDI 1996):

$$\sigma = \frac{150 \cdot V_a}{\pi} \cdot \left[\frac{(1/R^2 - 1) \cdot 2C \cdot \cos(\theta)}{F_0 \cdot D} \right] \quad (1)$$

120 For our 2-pulse system the ideal correlation R is 0.5, speed of sound C is 1440 m s^{-1} , and the
121 standard deviation σ becomes 0.096 m s^{-1} . This uncertainty is reduced as $M^{-1/2}$ for M indepen-
122 dent pings. The ADCPs of Design-A sampled $M=40$ acoustic pings every two hours while the
123 ADCPs of Design-B sampled 120 velocity pings every half hour. We thus estimate measurement
124 uncertainties of 0.015 and 0.009 m s^{-1} for Design-A and B, respectively.

125 Scatterers appear intermittently during the winter below the sea ice causing gaps in the data.
126 We fill gaps shorter than a day by interpolating velocities in time for each vertical bin. First, we
127 replace all 'bad' velocity values with tidal predictions that we determine from the 'good' values.
128 The tidal fit includes 4 semi-diurnal (M_2 , S_2 , N_2 , K_2) and 3 diurnal (K_1 , O_1 , P_1) components.
129 Second, for every daily interval with more than 8 hourly values, we interpolate missing values
130 for each 24 hour segment after the tidal predictions are removed. The first step fills all gaps with
131 a small albeit deterministic current oscillation. The second step fills gaps shorter than 16 hours
132 with a biharmonic spline using only detided 'good' velocity estimates. The tides are added back
133 after the spline interpolation. This procedure removes all data gaps. In a final step, the time
134 series are filtered with a Lanczos raised cosine filter with a half-power point near 34 hours and
135 a window width of 75 hours to remove tidal and inertial oscillations (Walters and Heston 1982).
136 These filtered values are then subsampled into daily values that represent subtidal ocean current
137 variability.

138 Estimating uncertainty for speed and direction of ocean currents, we use 95% confidence levels
139 (Table 2). Speed estimates are assumed to originate from a Gaussian distribution where velocity
140 vectors have a decorrelation time scale T_d that varies between 4 and 12 days depending on location.
141 We determine T_d from a lagged auto-covariance function that we integrate to its first zero crossing
142 following procedures introduced by Kundu and Allen (1976). Uncertainty in directions are 95%
143 confidence limits from directional statistics that use the von Mises' probability distribution on a

144 unit circle from which a mean resultant length R of current vectors on a unit circle (Mardia 1972)
145 are used.

146 During mooring deployment in June 2014 and recovery in August 2016 we measured ocean
147 water properties with a SeaBird 911⁺ conductivity-temperature-depth (CTD) sensor package that
148 was calibrated at the factory a few month prior and after each expedition (Kanzow et al. 2017;
149 Schaffer et al. 2017). Salinity estimates were compared at sea against measured salinities from
150 discrete water samples via salinometer.

151 Atmospheric observations are available from the Danish Meteorological Institute at Station
152 Nord (81.6° N, 16.7° W), Hendrik Krøyer Holme Island (80.7° N, 13.7° W), and Danmark
153 Havn (76.8° N, 18.7° W). Fig. 1 shows that both Station Nord and Danmark Havn are lo-
154 cated near mountainous terrain and wind vectors from these stations do not necessarily repre-
155 sent conditions on the continental shelf, however, more representative daily wind observations
156 are available from an automated weather station on uninhabited Hendrik Krøyer Holme Is-
157 land. For the 822 days of our study period from 1 June, 2014 through 31 August 2016 we have
158 695 daily wind observations at Hendrik Krøyer Holme Island. These wind and air temperature
159 data are accessed from NOAA's National Centers for Environmental Information as hourly val-
160 ues (<https://www.ncei.noaa.gov/data/>) that we bin into daily averages. The observations compare
161 favorably to estimates from the European Center for Medium-Range Weather Forecasting ERA-
162 Interim Reanalysis products (Dee et al. 2011) of 10-m wind vectors and 2-m air temperatures (not
163 shown).

164 Remotely sensed surface conditions originate from daily observations of microwave SSM/I and
165 optical MODIS satellites, respectively. We use SSM/I sea ice concentrations data from NSIDC
166 archives at 25 km resolution (Steffen and Schweiger 1991) while MODIS data are surface re-
167 flectance at 865 nm obtained from NASA's Goddard Space Flight Center at 250 m resolution.

168 **3. Sea Ice and Atmospheric Conditions**

169 In polar regions the distribution of sea ice in time and space determines how the atmosphere
170 forces the ocean in at least two ways. Mobile sea ice can enhance the frictional coupling and thus
171 momentum flux between atmosphere and the ocean, because the roughness elements of ridged
172 sea ice are larger than that of an ice free sea surface (Lübkes and Birnbaum 2005; Martin et al.
173 2014; Schulze and Pickart 2012). In contrast when densely packed sea ice becomes less mobile,
174 then it can shut down local wind forcing completely as it does in winter over coastal areas of the
175 North-East Greenland continental shelf (Hughes et al. 2011). Hence we next provide a description
176 of sea ice and winds to reveal the seasonality that impacts our ocean current observations.

177 Sea ice covers most of the North-East Greenland shelf for most of the year. Fig. 2a shows a time
178 series of daily sea ice concentrations. We quantify the sea ice cover by averaging daily SSM/I
179 passive microwave data over an area that includes our mooring locations (Fig. 1). From October
180 through June in 2015 and 2016 we find that about 85% of our study area is covered by sea ice
181 (Fig. 2a). The sea ice minimum occurs the last two weeks in August when only about 20% of our
182 area is covered by mobile sea ice (Fig. 3). Ice-cover diminishes slowly for 2 months in June and
183 July as a result of sea ice melting and dispersal, but it reforms rapidly within 2 weeks in October
184 of 2014 and within 4 weeks in September and October of 2015.

185 Visualizing the spatial sea ice distribution, we show in Fig. 3 two MODIS Terra images. The
186 first image on 15 June 2014 coincides with the mooring deployment in partially open water with
187 many large and mobile floes. About 80 km to the north and west, however, the ice cover is 100%
188 and immobile, that is, landfast sea ice covers a coastal area about 100 km wide and 250 km long
189 between 78° and 80° N latitude. We indicate this area by the yellow contour in Fig. 3 that we
190 also use as an estimate of maximal extent of the landfast sea ice. In years past, this landfast ice

191 survived the entire summer (Hughes et al. 2011), however, this is no longer the case (Hughes et al.
192 2011; Sneed and Hamilton 2016). The image of 30 August 2014 depicts a small remnant of this
193 landfast sea ice in the form of a roughly 80 km long and 30 km wide segment near 79° N and
194 14° W (Fig. 3). Most of the shelf area in August, however, is covered by mobile sea ice. Unlike
195 winter, the summer sea ice is mobile as it is advected and dispersed by winds and ocean currents
196 while it melts in response to solar heating.

197 Air temperatures over the ocean range from -30 °C in October to May and reach +10 °C in
198 July to August (Fig. 2c). We estimate seasonal air temperatures by fitting observations against
199 $T_{air}(t) = T_0 + T_1 * \cos(\omega t - \phi)$ where ω represents the known annual frequency and T_1 and ϕ the
200 amplitude and phase of the annual cycle. Minimizing the least squares between data and fit, we
201 find that the mean temperature is $T_0 = -10.2 \pm 0.6$ °C that varies seasonally by $T_1 = 10.8 \pm 1.2$
202 °C. The phase indicates temperature maxima on about 25th July. Uncertainties are 95% confidence
203 limits assuming Gaussian noise and a decorrelation time scale of 4 days.

204 Observed wind vectors on Hendrik Krøyer Holme Island appear largely in-phase with air tem-
205 peratures. Largest winds to the south coincide with minimal air temperatures on about 25th of Jan-
206 uary. Seasonal wind variations have an amplitude of 4.2 ± 1.8 $m s^{-1}$ about the mean of 3.5 ± 0.9
207 $m s^{-1}$ along the north-south principal axis of variation (Fig. 2b). Note that observed winds during
208 the cold season frequently exceed $20 m s^{-1}$ over the generally land-fast sea ice on the continental
209 shelf. Strong but short-lived warming events occur in winter such as in Nov.-2014, Apr.-2015, and
210 Feb.-2016 when winds from the north reverse and bring warm air from open Fram Strait waters in
211 the south-east.

212 **4. Hydrography**

213 Schaffer et al. (2017) reviews all available hydrography for the entire shelf area to note sub-
214 surface temperature maxima in the 800 km long trough system between 76° and 80° N latitude.
215 Averaging data into 100 km bins along the trough system below 200-m depth, they find waters
216 during the 2000-16 period to be about 0.5°C warmer than those observed during the 1979-99
217 period. In contrast, we here focus on the vertical and across-slope structure of the temperature
218 and salinity fields. Figs. 4 and 5 show 2014 and 2016 summer snapshots of the local hydrogra-
219 phy, respectively, along with measurement locations of both CTD survey and ADCP mooring data
220 labeled M10 through M70 (Table 1).

221 In both 2014 and 2016 we find the warmest waters below 250 m depth adjacent to the north-
222 eastern rim of the trough system. In June of 2014 (Fig. 4) potential temperatures reach values
223 above $+1.5^\circ\text{C}$ almost across the entire section at depths below 300 m, but temperatures reach $+1.7$
224 $^\circ\text{C}$ for a CTD cast at km-75. The salinity distributions are almost level across the section except
225 for a 5-km wide area over the north-eastern slope at km-85 where we will find the core of the
226 subsurface jet. Maximal ocean temperatures in August of 2016 are $+1.8^\circ\text{C}$ near 300 m depth (Fig.
227 5). The subsurface temperature maximum appears as a 15 km wide and 50 m thick intrusion that
228 is attached to the north-eastern rim of the canyon. Furthermore, we find upward sloping salinity
229 contours near km-80 within which the local temperature maximum is embedded. Dynamically
230 this is consistent with a northward geostrophic flow below 150 m depth relative to a weaker flow
231 at the surface. Temperature time series within about 3 m off the bottom (not shown) indicate that
232 these patterns persist throughout the year, that is, seasonal variations are small and negligible.

233 5. Ocean Circulation

234 *a. Mean flow and volume flux*

235 The data from this array of seven ocean current moorings describe a jet over the north-eastern
236 slope of Norske Trough whose depth- and time-averaged representation we show in Fig. 3 and
237 list with uncertainties in Table 2. Fig. 6 shows the record-mean velocity along the canyon for
238 the three north-eastern mooring sites M50, M60, and M70. The flow constitutes a 10 km wide
239 bottom intensified jet towards coastal glaciers in the north-west. The velocity maximum exceeds
240 0.08 m s^{-1} near 300 m depth and diminishes towards both the surface and the channel center (Fig.
241 6). This bottom-intensified flow is the main circulation feature to dominates both the time mean
242 and the time-domain variability.

243 Spatial patterns coherent to all records from all 7 mooring locations reveal that more than 36% of
244 the total variance is contained within the principal pattern (not shown) that has its maximal value
245 150 m below the surface at mooring sites M50, M60, and M70 over the north-eastern slope of
246 Norske Trough. The data from the south-western 4 moorings contribute little to this mode. Hence
247 we subsequently focus on the spatial and temporal variability of this north-eastern slope current
248 that advects warm waters of Atlantic origin across the continental shelf of North-East Greenland.

249 Fig. 7 shows the volume flux $Q(t)$ of Atlantic influenced waters that we define as those with
250 salinities larger than 34 psu. This isohaline is almost level across the section at 150-m depth (Figs.
251 4 and 5). Estimating volume transport, we generate regular grids of daily velocity $u(x,z,t)$ that we
252 integrate vertically from the bottom at $H(x)$ to 150 m depth and horizontally from $x_1 = 75 \text{ km}$ to
253 $x_2 = 90 \text{ km}$, e.g.,

$$Q(t) = \int_{x_1}^{x_2} \int_{-H(x)}^{-150} u(x, z, t) dz dx. \quad (2)$$

254 The record-mean volume flux Q_0 becomes 0.27 ± 0.06 Sv ($10^6 m^3 s^{-1}$). Uncertainties are 95%
255 confidence limits assuming an integral time scale of about 11 days. Also shown in Fig. 7 are the
256 2-day low-pass and 19-21 day band-pass filtered data. Volume flux values including the temporal
257 mean range from -0.4 to +1.4 Sv for the low-pass and from +0.0 to to +0.6 Sv for the band-pass
258 data. Positive flux is to the north-west towards coastal glaciers. Next we detail vertical and lateral
259 structures of this along-slope current.

260 *b. Vertical Velocity Variations*

261 In Fig. 8 we show current vector time series at the core of the slope jet at five selected depths
262 between 39 m and 335 m below the generally ice-covered surface. The flow below 150 m depth
263 is remarkably steady and to the northwest towards the coast. Current reversals are few and short-
264 lived. Seasonal variations emerge and their amplitudes determined from a harmonic analysis (not
265 shown) increase from less than $0.015 m s^{-1}$ near the bottom to almost $0.06 m s^{-1}$ at 143 m (not
266 shown). Strongest seasonal flow to the north occurs in December/January and weaker flow in
267 June/July. Both the time mean flow and variations align along an axis close to 319 degrees clock-
268 wise from true North that we subsequently select as the along-canyon direction. We will next
269 quantify mean, seasonal, and residual sub-inertial currents. The latter we will decompose into
270 dominant empirical orthogonal modes.

271 Fig. 9 depicts the record-mean vertical profile at M60 separated into along-canyon and across-
272 canyon components. Within about 150 m of the surface both along- and across-channel speeds are
273 about $0.04 m s^{-1}$ with uncertainties of about $0.02 m s^{-1}$. The positive across-channel velocity is
274 a flow to the west which is dynamically consistent with the geostrophic adjustment to a frictional
275 Ekman-like response to winds generally blowing from the north, e.g., Fig. 2b. At depths below
276 150 m the across-channel velocity component vanishes while the along-channel component in-

277 creases to a maximum of $0.10 \pm 0.01 \text{ m s}^{-1}$ near 325 m depths. Below this depth currents along the
278 topography reduce towards the bottom with a small across-channel component down-slope that is
279 dynamically consistent with a frictional Ekman-like response also, but the down-slope flow here
280 is imposed by the along-channel current above.

281 The temperature structure on both 10-June-2014 and 16-August-2016 reveal 150-m thick surface
282 layers that consists of uniformly cold ($-1.6 \text{ }^\circ\text{C}$) waters where salinity stratifies the water (Figs. 4
283 and 5) and the time mean flow is dominantly across topography. Below this halocline layer we find
284 a thermocline layer between 150 and 300 m depth that has a constant temperature gradient of about
285 $2.8 \text{ }^\circ\text{C}$ per 150 m. Vertical current shear is largest within this thermocline layer as we approach
286 both the vertical temperature and velocity maximum below 300-m depth. Here the waters are
287 uniformly warm, ($+1.3 \text{ }^\circ\text{C}$) and salty (34.8 psu). The core of the the bottom-intensified jet thus
288 advects heat from Fram Strait across the shelf towards the coast.

289 *c. Time-dependent Currents*

290 Removing the mean currents at each depth, we next describe principal patterns of variability
291 in the along-channel direction with empirical orthogonal functions (EOF) as these constitute the
292 most efficient presentation of variability (Davis 1976). More specifically, EOF analyses quantify
293 the distribution of variance among a set of mutually uncorrelated patterns in space and how these
294 spatial patterns vary in time. We decompose 45 time series of along-channel velocity observations
295 $u(z,t)$ at M60 (see Fig. 9 for locations) into $M=45$ modes via the linear transformation

$$u(z_i, t) = \sum_{n=1}^M A_n(t) \cdot \theta_n(z_i) \quad (3)$$

296 where $A_n(t)$ and $\theta_n(z_i)$ denote the temporal amplitude and vertical pattern of the n-th EOF mode,
297 respectively. We scale $A_n(t)$ and $\theta_n(z_i)$ such that $A_n(t)$ is dimensionless with variance 1 and $\theta_n(z_i)$
298 has units of $cm s^{-1}$. Appendix-B explains the details.

299 From 45 distinct eigenvectors $\theta_n(z)$ we find that θ_1 , θ_2 , and θ_3 dominate as they explain about
300 95% of the total velocity variance. Fig. 10 shows these three dominant modes and we limit
301 our discussion to them. The first mode explains 77% of the variance and its vertical structure
302 resembles the time-mean bottom-intensified flow. This first EOF has a peak velocity of about
303 $0.08 m s^{-1}$ at 180-m depth with strong vertical shear towards zero above this depth and little shear
304 towards the bottom (Fig. 10a). The flow within 100-m of the surface does not contribute much
305 to this EOF which contrasts with the next two modes. Mode-2 reflects a balanced exchange flow
306 for which surface and bottom currents are anti-correlated, that is, a flow towards the coast at the
307 surface coincides with a bottom flow in the opposite direction and vice versa. This exchange mode
308 captures about 15% of the total variance. An intensified surface flow in the upper 100-m of the
309 water column is described by mode-3, however, this mode contains only 4% of the total variance
310 and thus can be neglected along with higher modes not shown.

311 We note that the time scales of the bottom-intensified flow A_1 , the exchange flow A_2 , and the sur-
312 face intensified flow A_3 differ. Fig. 11 presents auto-spectral estimates of the temporal variations
313 $A_1(t)$ and $A_2(t)$ that for A_1 reveal three clear spectral peaks near 6, 11, and 20 day periodicities.
314 Signals with these time scales each contain more than 15% of the total variance and represent the
315 principal time scales at which the bottom-intensified jet varies about its mean. The second mode
316 A_2 has a single distinct peak near 20 days and contains most of its variance at periodicities larger
317 than 60 days (0.016 cycles per day or cpd below). We speculate that seasonally variable sea-ice
318 and winds causes these variations expressed in A_2 and θ_2 . Identical analyses for the data from ad-
319 jacent upslope and downslope moorings M70 and M50 reveal similar results (not shown). We thus

320 find similar vertical flow structures and time scales of variability from EOF analyses. We next
 321 investigate the across-canyon correlation of these flow structures with a linear systems analysis
 322 that will reveal wave-like properties of observed current fluctuations.

323 *d. Topographic Rossby Wave*

324 We estimate spectral properties from 2-year time series at M50 and M60 at 309-m and 303-m
 325 depth, respectively, because these two time series are both within the core of the warm subsurface
 326 jet (Fig. 6). A frequency-domain linear system $Y = H * X$ uses M60 as input X with an auto-
 327 spectrum G_{xx} and M50 as output Y with an auto-spectrum G_{yy} . The auto-spectra are real functions
 328 of frequency f that estimate the kinetic energy per frequency interval. In contrast the transfer
 329 function $H = |H|e^{-j\Theta_{xy}}$ is complex and thus carries both amplitude and phase information. The
 330 phase is estimated from the complex cross-spectrum $G_{xy} = |G_{xy}|e^{-j\Theta_{xy}}$ (Bendat and Piersol 1986).
 331 We use G_{xy} to aid in the interpretation of oscillatory motions with enhanced kinetic energies near
 332 periodicities of 20, 11, and 6 days (Fig. 11). More specifically, across-slope phase relations and
 333 principal axes of variations implicate topographic Rossby waves (Pickart and Watts 1990) as a
 334 possible explanation of the observed current oscillations. We discuss wave properties below after
 335 we quantify the phase propagation across the slope of signals that are coherent at M60 and M50.

336 Fig. 12 shows the phase $\Theta_{xy}(f)$ for $f \leq 0.3$ cpd. We find $\Theta_{xy} > 0$, that is, oscillations occur first
 337 at M60 before they appear at M50. For example, at 0.05 cpd a phase $\Theta_{xy} = 30$ degrees indicates
 338 that a signal takes 40 hours to reach M50 from M60. This corresponds to phase speed $c_p =$
 339 $(1/T)(360/\Theta_{xy})(\Delta s / \cos\Delta) = 3.2$ km/day for a wave with period $T=20$ days, site separation $\Delta s=5.3$
 340 km, and the angle $\Delta = 1$ degrees between the mooring line (39T) and the orientation of the wave
 341 number vector (Pickart and Watts 1990). The implied wavelength is $\lambda = c_p \cdot T = 63$ km.

342 How much of the variance of this 63-km across-slope scale at location M60 relates in this "linear
 343 wave fashion" to the variance at location M50? Fig. 12 suggests about 70%, because the coherence
 344 $\Gamma^2 = |G_{xy}|^2 / (G_{xx} G_{yy})$ estimates the fraction of the input variance related linearly to the output
 345 variance. The coherence Γ^2 reaches almost 0.7 at the relevant frequencies between 0.01 and 0.3
 346 cpd (Fig. 12). This value is far above the 95% confidence level of 0.15. We next compare these
 347 coherent observations with predictions from linear wave theory.

348 The dispersion relation of linear internal waves on a rotating plane in the presence of a bottom
 349 slope relates the wave frequency $\omega = 2\pi/T$ to the wave number $K = 2\pi/\lambda$ as

$$\omega(K) = -\frac{N \cdot \alpha \cdot \sin\phi}{\tanh(K \cdot L_D)} \quad (4)$$

350 that defines topographic Rossby waves (Gill 1982; Rhines 1970). Here N is the stability or Brunt-
 351 Väisälä frequency (0.005 s^{-1}), D is a vertical scale of motion (400-m), α is the bottom slope
 352 (0.03), and $\sin\phi = k/K$ indicates the orientation of the wave number vector $\vec{k} = (k, l)$ with magni-
 353 tude $K = \sqrt{k^2 + l^2}$ and components k along and l across the bottom topography. The parameter
 354 $L_D = N \cdot D / f_0 = 14 \text{ km}$ is the internal Rossby radius of deformation and f_0 is the local Coriolis
 355 parameter (0.00014 s^{-1}).

356 The waves are transverse, that is, they have $\vec{k} \cdot \vec{u} = 0$ where \vec{u} is flow velocity associated with
 357 the wave (Rhines 1970). Thus we can interpret the angle $\phi + \pi/2$ as the orientation of the current
 358 ellipse (Pickart and Watts 1990; Harden and Pickart 2018). The minus sign in Equation 4 indicates
 359 that waves propagate with shallower water to the right in the northern hemisphere, that is, the wave
 360 moves its perturbations along \vec{k} across topography from shallow to deep water. The restoring force
 361 is the vortex tube stretching over a sloping bottom in the presence of both rotation and stratification
 362 (Zhao and Timmermans 2018).

363 For the observed wavelength of 63 km and period of 20 days the dispersion relation Equation
 364 4 predicts the angle $\phi = 179$ degrees that is the direction of the phase velocity relative to ups-
 365 lope. We can compare this prediction against the orientation of the observed current ellipse at this
 366 frequency, because the wave number is always perpendicular to the current vector. We estimate
 367 current ellipses from band-pass filtered velocity data and list both observed and estimated wave
 368 properties in Table 3 for waves with periods near 20, 11, and 6 days.

369 Fig. 13 shows our co-ordinate system that we orient along (x) and across (y) the local topog-
 370 raphy. We also show current ellipses near 220 m depth at three locations across the slope. The
 371 deviation of the semi-major axis of length R_{maj} from the along-slope direction constitutes the
 372 observational estimate of the angle ϕ_{obs} measured from the across-slope direction. Analytical pre-
 373 dictions of ϕ from the dispersion relation, e.g., ϕ_{ana} agree with those derived directly from the
 374 observed, band-passed flow field, e.g., ϕ_{obs} (Table 3). The phase velocity vector is almost perpen-
 375 dicular to the topography, that is, the principal axis of current oscillations is almost along topog-
 376 raphy. This is a characteristic of short and strongly stratified Rossby waves where $\tanh(KL_D) \sim 1$
 377 (Pickart and Watts 1990). The bottom slope traps wave energy, that is, velocity variance near the
 378 bottom exceeds that near the surface. Velocity profiles vary as $\cosh(\mu z)$ in the vertical z-coordinate
 379 (Rhines 1970) where $\mu^{-1} = D/(KL_D)$ ranges from about 200 to 300 m for our waves (Table 3).
 380 Furthermore, we find, as expected from linear wave theory, that the angles $\phi_{obs} = \phi_{obs}(\omega)$ rotate
 381 clockwise with increasing ω , i.e., higher frequency motions propagate perturbations with more of
 382 an along-slope component than lower frequency motions. We note, however, that all these angles
 383 are small as the along-slope component of the wavenumber k is much smaller than the across-slope
 384 component l , that is, $k \ll l$.

385 6. Forcing

386 For stratified topographic Rossby waves with $K \cdot L_D \gg 1$ the dispersion relation simplifies to

387 $\omega(K) \approx -N \cdot \alpha \cdot \sin\phi$. From this approximation we find the group velocity vector

$$\vec{c}_g = (\partial_k \omega, \partial_l \omega) = c_0 \cdot (-\cos\phi, \sin\phi) \quad (5)$$

388 where $c_0 = (N \cdot \alpha \cdot \cos\phi / K)$ and $\cos\phi = l / K$ (Harden and Pickart 2018). Fig. 13 shows \vec{c}_g for the

389 19.3 day oscillation. The speed of the energy flux vector \vec{c}_g is 63 km/day and it is directed into the

390 Norske Trough system from offshore Fram Strait towards the coastal glaciers in the north-west.

391 Hence we must seek the energy source for our observed wave motions to the south-east of our

392 study area where the trough system broadens and merges with the slope of the outer continental

393 shelf and Fram Strait. Here the ice cover is mobile all year and allows for efficient momentum

394 transfer from the atmosphere to the ocean.

395 Our observed topographic Rossby waves depend on vertical density stratification N and a sloping

396 bottom α , e.g., $\omega = \omega(N, \alpha)$ that both provide the restoring mechanism for wave perturbations via

397 vortex tube stretching in a baroclinic fluid. The curl of the surface wind stress perturbs the density

398 field via an Ekman pumping velocity w_e (Gill 1982)

$$w_e = (\partial_x \tau^{(y)} - \partial_y \tau^{(x)}) / (\rho_0 \cdot f_0) \quad (6)$$

399 and this density perturbation, we postulate, then travels as the topographic Rossby wave whose

400 properties we list in Table 3. Appendix C describes details of our wind stress estimation in ice-

401 covered seas that use ERA interim wind and SSM/I sea ice products at daily and 25-km scales.

402 Fig. 14 shows a snapshot of the spatial wind variability during a particular strong event on

403 17th December of 2015 when cyclonic winds reach 20 m s^{-1} in Fram Strait just seaward of the

404 1000-m isobath. In contrast, near our mooring location wind speeds are less than 5 m s^{-1} . The

405 vertical upwelling is maximal near the continental slope while it is close to zero at our mooring

406 site. Bottom-intensified ocean currents at the time are two standard deviations above the mean as
407 expressed in the first EOF at M60 (Fig. 10).

408 Searching more systematically for a source location of the topographic Rossby wave generation,
409 we correlate our ocean current time series with Ekman pumping time series at all locations. The
410 correlation is done for signals in the narrow [19, 21] day band in the frequency domain where we
411 find enhanced kinetic energy (Fig. 11). The correlation then becomes $\Gamma^2(x,y)$ for $\omega = const.$ that
412 we map in Fig. 15. While statistically significant coherences Γ^2 are found scattered throughout
413 the study area, we indeed find the largest coherence $\Gamma^2 > 0.4$ in a 100 km long and 50 km wide
414 band over the shelf break near the 1000 m isobath where Norske Trough connects to Fram Strait.
415 We will next take a closer look at the data from this location to quantify the distribution of Ekman
416 pumping and how it correlates with velocity fluctuations that include our topographic Rossby
417 waves.

418 The Ekman pumping velocity $w_e(x = 8^\circ W, y = 76.5^\circ N, t)$ contains enhanced variance at pe-
419 riodicities near 20, 11, 6, and 4.5 days as shown by the power spectral density (Fig. 16). The
420 spectral peaks are similar to those we find in the spectra of bottom currents in Norske Trough (Fig.
421 11) that correlate across the slope with $\Gamma^2 \sim 0.7$ (Fig. 12). Estimating the coherence of bottom
422 currents in Norske Trough and Ekman pumping near the shelf break about 180 km to the east, we
423 find that the correlated variance at the 20 day time scale exceeds 40%. This is well above the 99%
424 confidence level $\Gamma_{99}^2 = 0.23$ for 40 degrees of freedom. Note also that the correlation of the signals
425 with frequencies between 0.15 and 0.07 cycles per day (7-14 days) falls below this significance
426 level. Currents at these frequencies thus are not correlated to Ekman pumping at a 99% level of
427 confidence. Hence we suggest that only low-frequency bottom currents in Norske Trough with pe-
428 riods near 19-21 and 5-6 days are forced remotely by the wind-stress curl near sloping topography
429 of Fram Strait. The kinetic energy generated by the wind stress curl propagates with the group

430 velocity of a baroclinic Rossby wave along the sloping topography to cause along-slope velocity
431 oscillations at 20 day periodicities.

432 Furthermore, the correlated variance suggest a linear input-output system: Bottom currents lag
433 the Ekman pumping by about 70 degrees or about 4 days at a 20-day period. This lag translates
434 to a speed of 45 km/day for the 180 km distance between these locations. Visualizing this phase
435 lag, we show in Fig. 17 band-pass filtered time series of Ekman pumping at two select locations
436 (shown in Fig. 14) that we each overlay with similar band-pass-filtered bottom velocity at M60.
437 Prominent bottom velocity oscillations with amplitudes near 0.1 ms^{-1} emerge in November of
438 2015 that persist through February of 2016. The visual correlation is strong at the shelfbreak for
439 the w_e at 7°W (bottom panel of Fig. 17) while it is weak at the mooring locations near 15°W (top
440 panel of Fig. 17). The winter 2015/16 Ekman pumping near the 1000 m isobath of Fram Strait has
441 an amplitude of about 0.4 m/day from which our linear system analysis gives a gain (not shown)
442 of 19 (cm/s)/(m/day) for both the 20 and 6 day oscillations. Positive w_e (downwelling) in Fram
443 Strait leads negative along-slope bottom velocities (landward) in Norske Trough. Note, however,
444 that we present gain, phase, and coherence in the frequency domain and we thus weight all data
445 from the entire 945 day long time series equally.

446 7. Discussion and Conclusions

447 We introduced ocean current time series from a single array of 7 moorings that each contained
448 a vertically profiling ADCP that returned data from June 2014 through August 2016. The data
449 described the flow field within an 80 km wide canyon off North-East Greenland that connects
450 Fram Strait offshore with tidewater glaciers inshore. The array sampled a single section across
451 Norske Trough with distinct circulations on each side of the sloping canyon. We focused on a

452 bottom-intensified jet over the north-eastern slope that advects warm waters of Atlantic origin
453 from Fram Strait across the continental shelf via Norske Trough.

454 Sub-tidal flows exceed 0.2 m s^{-1} and are remarkably steady especially below 150 m depth where
455 they flux a volume of $0.27 \pm 0.06 \text{ Sv}$ towards coastal glaciers. Currents are highly correlated both
456 vertically and across the north-eastern slope. Maximal mean values occur 50-100 m above the
457 bottom in 400 m deep water. They are directed along the slope towards the coast in the north-
458 west. A single dominant EOF mode captures about 77% of the variance at each of three mooring
459 locations that describes the sub-surface jet. Jet amplitudes average about 0.1 m s^{-1} , but amplitudes
460 twice this value occur 2-3 times during the winter of 2014/15 and 2015/16.

461 Variability about the seasonal cycle is minimal in summer (Fig. 10) when the sea ice cover is
462 mobile, but local winds are weak. In contrast variability is maximal during December and January
463 when the sea ice is less mobile or even landfast over much of the coastal continental shelf, but both
464 winds and wind-stress curl are maximal, especially seaward from our measurement locations.

465 Spectral analyses of temporal EOF amplitudes suggest that variance of the subsurface jet has
466 distinct peaks at 20, 11, and 6 day time scales. Furthermore, we find that about 70-75% of the
467 ocean current variance at these time scales correlates across the sloping topography. This high
468 correlation gives stable estimates of the phase relation of oscillatory signals. More specifically,
469 correlated signals propagate from shallow into deep water with speeds ranging from about 3.2
470 km/day near 20 days to 6.8 km/day near 6 days periodicities (Table 3).

471 We interpret these propagation speeds as phase velocities of linear topographic Rossby waves
472 (Pickart and Watts 1990; Harden and Pickart 2018) that have wave lengths between 93 km (6.5
473 days) and 131 km (19.3 days). Comparing estimated angles of the wave vector relative to the
474 orientation of the topography against those predicted from linear Rossby wave theory (Rhines
475 1970), we find excellent agreement even though both observed and predicted angles are small,

476 about 1-4 degrees from upslope. The observations also reveal smaller angles for lower frequencies
 477 which is a property predicted by linear theory that is not always observed consistently (Pickart and
 478 Watts 1990; Kanzow and Zenk 2014). Some of our agreements with theory are likely fortuitous,
 479 however, because random errors impact our estimates of the orientation of the wave number vector.
 480 For example, we do not know the orientation of the topography well enough to ensure phase
 481 propagation with shallow water on the right as required in the northern hemisphere.

482 Furthermore, cross-spectral estimates have phase uncertainties larger than 2 degrees and non-
 483 steady wave scattering may occur along irregular smaller scale topography. Nevertheless, our
 484 quantitative wave estimates are consistent within the array and agree well with linear wave theory
 485 that predicts a group velocity of about 63 km/day along the slope towards the coast. This suggests
 486 a wave generation source seaward from our mooring site. We identify the generation region as the
 487 area of high correlation of wind stress near the surface and ocean currents near the bottom. More
 488 than 50% of the Ekman pumping variance correlates with the along slope bottom currents more
 489 than 180 km away within the sloping canyon topography.

490 The dynamics appear linear, because Rossby numbers $Ro = \delta U / (f_0 \cdot \delta y) \ll 1$. Here we use the
 491 lateral velocity differences δU across the jet ($\sim 0.08 \text{ m s}^{-1}$) over a distance δy ($\sim 11 \text{ km}$) to find
 492 the lateral shear of about $0.05 \cdot f_0$ where f_0 is the local Coriolis parameter. The ratio of relative
 493 ($\xi \approx \delta U / \delta y$) to planetary (f_0) vorticity is thus small ($Ro \ll 1$) and nonlinear inertial terms in the
 494 momentum equations become negligible (Gill 1982). We neglect small variations of across-slope
 495 velocity δV along the slope. For small Rossby number the potential vorticity

$$PV = \frac{f_0 + \xi}{D} \approx \frac{f_0}{D} \quad (7)$$

496 where D is the vertical scale of motion. For unforced motions PV is conserved and the flow follows
 497 contours of f_0/D . Such flows are said to be topographically steered.

498 For barotropic motions D is the water depth H and the steady flow follows depth contours on
499 an f -plane. In contrast, our steady (mean) velocity observations are bottom-intensified below the
500 main pycnocline (Fig. 6). Hence our flow is baroclinic and D is the layer thickness below the
501 pycnocline. The flow can move into shallower or deeper water, but in order to conserve PV , the
502 pycnocline moves vertically in unison to keep D constant on an f -plane. In steady state the sloping
503 isopycnals will be geostrophically balanced, that is, a bottom-intensified flow moving over a sill
504 into deeper water will be turned or steered to keep shallow water on the right rather than moving
505 into deeper water.

506 We speculate that our bottom-intensified mean flow is topographically steered and enters Norske
507 Trough near 76.5° N from Fram Strait to the north of 77.5° N latitude (see Fig. 1). Håvik
508 et al. (2017) report similar waters, density structures, and velocities inshore of the shelfbreak East
509 Greenland Current (EGC). Fig. 18 compares temperature and salinities along this proposed path
510 from northern Fram Strait near 77.5° N inshore of the 400-m isobath to our mooring section in
511 the west via the entrance of Norske Trough in the east near 76.5° N latitude. The core of Atlantic
512 Waters are the temperature maxima near the 27.9 kg m^{-3} potential density anomaly. Over the
513 upstream continental slope this water has a temperature of 3°C while at the eastern entrance to
514 Norske Trough in the south its temperature maximum has cooled to 2.5°C . At our mooring section
515 in the west, we find this maximum near 1.9°C . The densities are almost identical which suggests
516 mixing with cooler and fresher waters. Coachman and Barnes (1963) presents similar data to
517 describe the circulation of Atlantic Waters in the Arctic Ocean by tracing the core of this water.

518 In summary, we posit that our observations describe a topographically steered mean flow near
519 the 400-m isobath, however, the heat of waters that enter Norske Trough and move it towards
520 coastal glaciers do not originate from the EGC. Instead, they originate from the upper continental
521 slope of Fram Strait inshore from the EGC.

522 The small Rossby numbers motivated our search for remotely forced baroclinic Rossby waves to
523 explain the temporal variations of the observed bottom intensification of currents over the slope at
524 a set of discrete periodicities. We find statistically significant phase propagation of ocean current
525 variability from shallow to deep water. These temporal oscillations modulate the mean flow at
526 periodicities of 20, 11, and 6 days. Properties of these oscillations are dynamically consistent with
527 the dispersion relation of topographic Rossby Waves where the bottom slope provides the main
528 restoring mechanism in our rotating and stratified fluid. These propagating waves can be generated
529 by any disturbance of the density field. A time-dependent meandering ambient flow such as the
530 EGC can generate perturbations that propagate as topographic Rossby Waves (Maslowski 1996).
531 The upwelling or downwelling caused by an eddy crashing into sloping bottom topography, too,
532 can generate topographic waves (LaCasce 1998). While we cannot offer a specific wave generation
533 process for the 11 day oscillation, we describe both a generation mechanism and location for our
534 20 and 6 day waves via Ekman pumping over the upper slope of Fram Strait.

535 The evidence presented supports the hypothesis that the wind-stress curl over the topographic
536 slope of Fram Strait generates baroclinic perturbations that reach our study area where we detect
537 them as bottom-intensified low-frequency current oscillations. Similar oscillations may exist far-
538 ther into Norske Trough and perhaps even 79N Glacier. It is unclear, however, if the decreasing
539 canyon width and/or its smooth change of orientation will affect the topographic Rossby waves.

540 The proposed Rossby wave generation differs from the upwelling and downwelling off East
541 Greenland described by Håvik and Våge (2018). Using the same ERA-Interim wind data as we
542 do here, Håvik and Våge (2018) find that coastal upwelling and downwelling favorable winds
543 cause across-shelf currents near the bottom that change the density below the East Greenland
544 Current at 68 °N latitude. Analyzing wind climatology, Håvik et al. (2017) suggest that this
545 process diminishes in importance north of 72 °N latitude.

546 Within 200 km of Denmark Strait Harden and Pickart (2018) interpret moored ocean current ob-
547 servations across sloping topography off northwest Iceland as topographic Rossby waves. These
548 waves are represented by the same dispersion relation that we use to describe current oscillations
549 within Norske Trough. Off Iceland the dominant Rossby wave has a period of ~ 4 days, wavelength
550 of ~ 60 km, and an offshore phase speed of ~ 17 km/day. The corresponding onshore group veloc-
551 ity of ~ 36 km/day suggests an offshore generation region. Harden and Pickart (2018) hypothesize
552 that a meandering East Greenland Current (Håvik et al. 2017) or aspiration of dense waters mov-
553 ing towards the sill of Denmark Strait 200 km away (Harden et al. 2016) may also contribute to
554 the Rossby wave generation. Hence while their observed wave is similar to ours, the generation
555 mechanism differs.

556 Our analysis bolsters a hypothesis that a carefully designed experiment can test: Ekman pumping
557 caused by the wind stress curl generates topographic Rossby waves over the strongly sloping
558 topography of the Fram Strait shelf break that propagate into canyons that cut across wide shelves
559 off north-east Greenland. The experimental design to test this hypothesis consists of an array of
560 bottom-mounted current meters spaced along the slope of the Norske Trough system from Fram
561 Strait to 79N Glacier. Similar physics may impact observable ocean current variability elsewhere
562 near sloping topography.

563 *Acknowledgments.* The National Science Foundation supported the initial fieldwork with OPP-
564 0230236 and analyses with OPP-1022843 (AM) while the Deutsche Forschungsgemeinschaft
565 funded JS and TK with KA-3204/5-1 as part of the Special Priority Program 1889 "Regional Sea
566 Level Change and Society." Both the University of Delaware and the Alfred-Wegener-Institute
567 provided substantial additional support with capital equipment and salaries. Instrument prepara-
568 tion, deployment, and recoveries were accomplished through dedicated efforts by a large group of

569 international scientists, engineers, and technicians that included Jonathan Poole and Mathias Mon-
570 sees. We also thank Captains and crews of R/V Polarstern during PS85 and PS100 as well as Drs.
571 Benjamin Rabe and Wilken Jon von Appen who supported mooring deployment and recoveries
572 in a safe, efficient, and enjoyable fashion. Drs. Paul Dodd and Laura de Steur of the Norwegian
573 Polar Institute helped with recovery and deployment of M71 and M72, respectively, in 2015. Two
574 reviewers provided detailed and constructive feedback that improved both text and figures.

575 APPENDIX A

576 **Compass Heading and Calibration**

577 Ocean current sensors generally use a flux gate compass to reference direction. While the mag-
578 netic field strength vector is constant at a fixed time, it is its horizontal component that turns the
579 "compass needle" as the sensor package changes orientation. This horizontal component decreases
580 with decreasing distance from the magnetic North Pole. In 2015 this pole was about 1100 km from
581 our study area where the horizontal component was only 7230 ± 130 nT for the 2014-16 period
582 of our observations. Furthermore, the local declination D_0 is 15.9 ± 0.8 degrees W and its drift
583 D_1 is about 0.46 degrees per year. We thus convert the magnetic compass heading M to true North
584 $T = M + D_0 + D_1 * t$ where time t is measured in years. We extracted numerical values from the
585 World Magnetic Model as distributed by NOAA's National Centers for Environmental Information
586 (<https://www.ngdc.noaa.gov/geomag>).

587 Our moored ocean current sensing array contains two different mooring designs that are listed in
588 Table 1. Design-A places the ADCP package on a mooring line that changes orientation as a result
589 of ocean current drag on the entire >200 m mooring line that accommodates additional sensors
590 and buoyancy elements. The ADCP is contained in a stainless steel frame and its batteries are

591 de-gaussed. This minimizes compass bias, but the sensor package changes orientation by ± 180
592 degrees in response to variable drag on the mooring.

593 In contrast, Design-B places the ADCP transducers atop a steel float 3-m off the seabed on a
594 semi-rigid frame that is allowed to pitch and roll, but cannot change orientation. Fig. A1 shows
595 25-month long time series of pitch, roll, heading and pressure at M20. It shows a stable mooring
596 platform with small pitch and roll near 0.5 degrees each with deviations from these means always
597 smaller than 0.4 degrees. The magnetic compass starts at about 86.5 degrees and declines at the
598 predicted rate $D_1=0.46$ degrees per year caused by the steady movement of the earth's magnetic
599 pole. Furthermore, we identify five spikes caused by geomagnetic storms of charged solar par-
600 ticles that also cause intense Northern Lights. Observations of these solar flares are distributed
601 by the National Geophysical Data Center (<https://www.ngdc.noaa.gov/stp>). The storms cause in-
602 termittent compass fluctuations of up to 4 degrees. Our records thus contain a random noise < 1
603 degrees. The compass on Design-A moorings contain the drift, solar perturbations, and random
604 fluctuations as well.

605 Münchow and Melling (2008) introduced this torsionally-rigid mooring Design-B in Nares Strait
606 where magnetic compasses are unreliable. The problem then becomes to determine the (unknown)
607 constant offset or bias of the instrument package that sits fixed on the ocean floor. In Nares Strait
608 0.5 m s^{-1} strong and rectilinear tidal currents provided a natural co-ordinate system in the 30 km
609 wide channel, however, no such current or channel exist in Norske Trough and a different method
610 is developed here to determine the unknown constant offset.

611 More specifically, we employ complex correlation analysis of our observed vector time series
612 with a reference time series. The reference vector time series originates from barotropic tidal
613 predictions made for the entire Arctic Ocean by Padman and Erofeeva (2004) that use 8 discrete
614 tidal constituents. Our observation-based vector time series results from a tidal harmonic analysis

615 of vertically averaged currents that use the same 8 discrete tidal constituents as the model predicts.
616 We thus quantify the constant offset angle from observed tidal current vectors $w_1 = u_1 + j \cdot v_1$ with
617 predicted tidal current vectors $w_2 = u_2 + j \cdot v_2$, where "j" represents the complex unit vector. The
618 complex correlation $c_{12} = (u_1 + j \cdot v_1) \cdot (u_2 - j \cdot v_2)$ can be decomposed into a magnitude and an
619 orientation in the complex plane. The orientation angle rotates w_2 into w_1 to result in maximal
620 correlation. Table 1 includes this angle at which input and output time series of current vectors
621 result in a maximal correlation.

622 We estimate directional uncertainties to be less than 0.5 degrees, because moorings M50 and
623 M71 result in offset angles of 0.6 and 0.1 degrees, respectively, following the above complex cor-
624 relation. These Design-A moorings do not require compass corrections as their absolute directions
625 are known. Furthermore, the largest uncertainty probably results from uncertain tidal currents in
626 the barotropic Padman and Erofeeva (2004) model that requires accurate bottom depths. Table 1
627 lists both actual and model depths: at M50 the model depth of 453 m agrees well with the actual
628 depth of 456 m. In contrast, a large depth discrepancy exists at M71 where the model uses 347 m
629 when the actual depth is only 250 m. Nevertheless, tidal predictions and observations agree within
630 0.1 degrees in direction.

631 APPENDIX B

632 Empirical Orthogonal Functions (EOF)

633 EOF analyses organize serial observations at multiple locations $u(t_k, x_j)$ as a set of mutually uncor-
634 related serial variations $A_n(t_k)$ where the spatial dependence is expressed via a structure function
635 $\theta_n(x_j)$. The transformation from the vector space of observations $u(t_k, x_j)$ to the vector space of

636 uncorrelated EOF modes is linear, that is,

$$u(x_j, t) = \sum_{n=1}^M A_n(t) \cdot \theta_n(x_j) \quad (\text{B1})$$

637 Both $\phi_n(x)$ and $A_n(t)$ are orthogonal in the sense that

$$\sum_{i=1}^M \phi_n(x_i) \cdot \theta_m(x_i) = \delta_{n,m} \quad (\text{B2})$$

638

$$1/K \sum_{k=1}^K A_n(t_k) \cdot A_m(t_k) = \lambda_n \cdot \delta_{n,m} \quad (\text{B3})$$

639 Here $\delta_{n,m}$ is the Kronecker Delta which takes on a value of 1 for $n = m$ and 0 for $n \neq m$.

640 This heuristic description of EOFs describes a formal eigenvector problem for the cross-

641 covariance matrix $R_{i,j} = \sum_{k=1}^K u_i(x_i, t_k) \cdot u_j(x_j, t_k)$, that is,

$$\sum_{j=1}^M R_{i,j} \cdot \theta_m(x_j) = \lambda_m \cdot \theta_m(x_i) \quad (\text{B4})$$

642 where θ_m is the eigenvector of $R_{i,j}$ for the eigenvalue λ_m . The sum of all eigenvalues $\sum_{m=1}^M \lambda_m =$

643 $\sum_{m=1}^M R_{m,m}$ represents the total variance which we use to normalize the eigenvalues. In Equation-

644 B1 we thus scale $A_n(t)$ and $\theta_n(x)$ such that the eigenvector $\theta_n(x)$ carries units of $cm s^{-1}$ while the

645 eigenfunction $A_n(t)$ carries no units and has a variance of 1 for all modes n .

646

APPENDIX C

647

Wind-stress in ice-covered seas

648 The curl of the surface wind stress generates vertical motion that deforms the ocean density field

649 via Ekman pumping w_e , i.e.,

$$w_e = (\partial_x \tau^{(y)} - \partial_y \tau^{(x)}) / (\rho_0 \cdot f_0). \quad (\text{C1})$$

650 We estimate the wind stress $\vec{\tau} = (\tau^{(x)}, \tau^{(y)})$ from the wind vector $\vec{U} = (U, V)$ as

$$\vec{\tau} = \rho_{air} \cdot C_D \cdot (U^2 + V^2)^{1/2} \cdot \vec{U} \quad (\text{C2})$$

651 with the density of air $\rho_{air} = 1.32 \text{ kg/m}^3$ and a drag coefficient C_D . We use daily surface wind
652 data provide by the European Centre for Medium-Range Weather Forecast as the ERA-interim
653 product (Dee et al. 2011) to estimate wind-stress, its curl, and related Ekman pumping to construct
654 time series and maps of $w_e(x, y, t)$. A spatially variable ice cover such as shown in Fig. 3 will result
655 in spatially variable drag coefficients C_D that reflect different efficiencies of the momentum transfer
656 from the atmosphere to the ocean (Martin et al. 2014). We here implement the parameterisation
657 introduced by Lübkes and Birnbaum (2005) that includes a form drag $C_f(A)$ as well as skin drag
658 at ice-ocean ($C_{ice} = 1.89 \times 10^{-3}$) and air-ocean ($C_{ocean} = 1.25 \times 10^{-3}$) interfaces, e.g.,

$$C_D = C_f(A) + A \cdot C_{ice} + (1 - A) \cdot C_{ocean}. \quad (\text{C3})$$

659 where A is the fractional sea ice cover that we take from daily SSM/I imagery at 25 km resolution
660 (Steffen and Schweiger 1991).

661 The parameterisation assumes freely-moving sea ice that we do not always encounter on the
662 continental shelf where sea ice becomes land-fast in coastal and shallow areas (Hughes et al. 2011).
663 We thus arbitrarily set $C_D = 0$ when more than 98% of a pixel is covered by sea ice ($A < 0.98$).

664 References

- 665 Allen, S. E., 1996: Topographically generated, subinertial flows within a finite length canyon. *J.*
666 *Phys. Oceanogr.*, **26** (8), 1608–1632.
- 667 Allen, S. E. and B. M. Hickey, 2010: Dynamics of advection-driven upwelling over a shelf break
668 submarine canyon. *J. Geophys. Res.*, **115**, C08 018.
- 669 Arndt, J. E., W. Jokat, B. Dorschel, R. Myklebust, J. A. Dowdeswell, and J. Evans, 2015:
670 A new bathymetry of the Northeast Greenland continental shelf: Constraints on glacial and

671 other processes. *Geochemistry, Geophysics, Geosystems*, **16 (10)**, 3733–3753, doi:10.1002/
672 2015GC005931.

673 Bendat, J. and A. Piersol, 1986: *Random data: analysis and measurement procedures*. 2nd Ed.,
674 John Wiley & Sons, New York, NY, 566 pp.

675 Bourke, R. H., J. L. Newton, R. G. Paquette, and M. D. Tunnicliffe, 1987: Circulation and water
676 masses of the East-Greenland Shelf. *J. Geophys. Res.*, **92 (C7)**, 6729–6740.

677 Budéus, G. and W. Schneider, 1995: On the hydrography of the Northeast Water Polynya. *J.*
678 *Geophys. Res.*, **100 (C3)**, 4287–4299, doi:10.1029/94JC02024.

679 Budéus, G., W. Schneider, and G. Kattner, 1997: Distribution and exchange of water masses in
680 the Northeast Water Polynya (Greenland Sea). *J. Mar. Sys.*, **10 (1-4)**, 123–138.

681 Carroll, D., et al., 2016: The impact of glacier geometry on meltwater plume structure and
682 submarine melt in Greenland fjords. *J. Geophys. Res.*, doi:10.1002/2016GL070170.1002/
683 2016GL070170.

684 Coachman, L.K., C.A. Barnes, 1963: The movement of Atlantic water in the Arctic Ocean. *Arctic*,
685 **16**, 9–16.

686 Davis, R. E., 1976: Predictability of sea surface temperature and sea level pressure anomalies over
687 the North Pacific Ocean. *J. Phys. Oceanogr.*, **6 (3)**, 249–266.

688 de Steur, L., E. Hansen, C. Mauritzen, A. Beszczynska-Möller, and E. Fahrbach, 2014: Impact of
689 recirculation on the East Greenland Current in Fram Strait: Results from moored current meter
690 measurements between 1997 and 2009. *Deep-Sea Res.*, **92**, 26–40.

691 Dee, D. P., et al., 2011: The ERA-Interim Reanalysis: Configuration and performance of the data
692 assimilation system. *Q.J.R. Meteorol. Soc.*, **137**, 553–597.

- 693 Duchon, C., 1979: Lanczos filtering in one and two dimensions. *J. Appl. Meteor.*, **18**, 1016–1022.
- 694 Freeland, H. J. and K. L. Denman, 1982: A topographically controlled upwelling center off south-
695 ern Vancouver Island. *J. Mar. Res.*, **40** (4), 1069–1093.
- 696 Gill, A., 1982: *Atmosphere-Ocean Dynamics*. Academic Press Inc., 662 pp.
- 697 Harden, B. and R. Pickart, 2018: High-frequency variability in the North Icelandic Jet. *J. Mar.*
698 *Res.*, **76**, 47–62.
- 699 Harden, B.E., and 13 other, 2016: Upstream sources of the Denmark Strait Overflow: Observations
700 from a high-resolution mooring array. *Deep-Sea Res.*, **112**, 94–112, doi:10.1016/j.dsr.2016.02.
701 007.
- 702 Hickey, B. M. and N. S. Banas, 2008: Why is the northern end of the California Current system
703 so productive? *Oceanography*, **21** (4), 90–107.
- 704 Holland, D. M., R. H. Thomas, B. De Young, M. H. Ribergaard, and B. Lyberth, 2008: Accel-
705 eration of Jakobshavn Isbrae triggered by warm subsurface ocean waters. *Nature Geoscience*,
706 **1** (10), 659–664.
- 707 Håvik, L., R. Pickart, K. Våge, D. Torres, A. Thurnherr, W. Beszczynska-Möller, Walczowski, and
708 W.-J. von Appen, 2017: Evolution of the East Greenland Current from Fram Strait to Denmark
709 Strait: Synoptic measurements from summer 2012. *J. Geophys. Res.*, **122**, 1974–1994, doi:
710 10.1002/2016JC012228.
- 711 Håvik, L. and K. Våge, 2018: Wind-driven coastal upwelling and downwelling in the Shelfbreak
712 East Greenland Current. *J. Geophys. Res.*, **123**, 6106–6115, doi:10.1029/2018JC014273.

713 Hughes, N. E., J. P. Wilkinson, and P. Wadhams, 2011: Multi-satellite sensor analysis of fast-ice
714 development in the Norske Oer Ice Barrier, northeast Greenland. *Annals of Glaciology*, **52** (57),
715 151–160.

716 Inall, M. E., T. Murray, F. R. Cottier, K. Scharrer, T. J. Boyd, K. J. Heywood, and S. L. Bevan,
717 2014: Oceanic heat delivery via Kangerdlugssuaq Fjord to the south-east Greenland ice sheet.
718 *J. Geophys. Res.*, **119** (2), 631–645.

719 Jackson, R. H., F. Straneo, and D. A. Sutherland, 2014: Externally forced fluctuations in ocean
720 temperature at Greenland glaciers in non-summer months. *Nature Geoscience*, **7** (7), 503–508.

721 Johnson, H., A. Münchow, K. Falkner, and H. Melling, 2011: Ocean circulation and properties in
722 Petermann Fjord, Greenland. *J. Geophys. Res.*, **116**, C01 003, doi:10.1029/2010JC006519.

723 Johnson, M. and H. J. Niebauer, 1995: The 1992 summer circulation in the Northeast Water
724 Polynya from acoustic Doppler current profiler measurements. *J. Geophys. Res.*, **100** (C3),
725 4301–4307.

726 Kanzow, T., W.-J. von Appen, J. Schaffer, E. Koehn, T. Tsubouchi, N. Wilson, and A. Wisotzki,
727 2017: Physical oceanography measured with CTD/Large volume watersampler-system dur-
728 ing POLARSTERN cruise PS100 (ARK-XXX/2). PANGAEA, doi:https://doi.org/10.1594/
729 PANGAEA.871025.

730 Kanzow, T. and W. Zenk, 2014: Structure and transport of the Iceland Scotland Overflow plume
731 along the Reykjanes Ridge in the Iceland Basin. *Deep-Sea Res.*, **86**, 82–93.

732 Kundu, P. and J. Allen, 1976: Some three-dimensional characteristics of low-frequency current
733 fluctuations near the Oregon coast. *J. Phys. Oceanogr.*, **6**, 181–199.

734 LaCasce, J.H., 1998: A geostrophic vortex over a slope. *J. Phys. Oceanogr.*, **28**, 2362–2381.

- 735 Lübkes, C. and B. Birnbaum, 2005: Surface drag in the Arctic marginal ice zone: A compar-
736 ison of parameterisation concepts. *Boundary-Layer Meteorology*, **117**, 179–211, doi:10.1007/
737 s10546-005-1445-8.
- 738 Mardia, K., 1972: *Statistics of directional data*. Academic Press, New York, NY.
- 739 Martin, T., M. Steele, and J. Zhang, 2014: Seasonality and long-term trend of Arctic Ocean surface
740 stress in a model. *J. Geophys. Res.*, **119**, 1723–2738, doi:2013JC009425.
- 741 Maslowski, W., 1996: Numerical simulations of topographic Rossby waves along the East Green-
742 land Front. *J. Geophys. Res.*, **101**, 8775–8787.
- 743 Mayer, C., N. Reeh, F. Jung-Rothenhausler, P. Huybrechts, and H. Oerter, 2000: The subglacial
744 cavity and implied dynamics under Nioghalvfjærdsfjorden Glacier, NE-Greenland. *Geophys.*
745 *Res. Let.*, **27 (15)**, 2289–2292.
- 746 Mayer, C., J. Schaffer, D. Hattermann, T., F. Hatterma, L. Krieger, P. Dodd, T. Kanzow, C. Lic-
747 ciulli, and C. Schannwell, 2018: Large ice loss variability at Nioghalvfjærdsfjorden Glacier,
748 Northeast-Greenland. *Nature Comm.*, 1–11, doi:10.1038/s41467-018-05180-x.
- 749 Mouginot, J., E. Rignot, B. Scheuchl, I. Fenty, A. Khazendar, M. Morlighem, A. Buzzi, and
750 J. Paden, 2015: Fast retreat of Zachariae Isstrom, Northeast Greenland. *Science*, **350 (6266)**,
751 1357–1361, doi:10.1126/science.aac7111.
- 752 Münchow, A., 2016: Volume and freshwater flux observations from Nares Strait to the west of
753 Greenland at daily time scales from 2003 to 2009. *J. Phys. Oceanogr.*, **46 (1)**, 141–157.
- 754 Münchow, A. and E.C. Carmack, 1997: Synoptic flow and density observations near an Arctic
755 shelf break. *J. Phys. Oceanogr.*, **27 (7)**, 1402–1419.

756 Münchow, A. and H. Melling, 2008: Ocean current observations from Nares Strait to the west of
757 Greenland: Interannual to tidal variability and forcing. *J. Mar. Res.*, **66** (6), 801–833.

758 Padman, L. and S. Erofeeva, 2004: A barotropic inverse tidal model for the Arctic Ocean. *Geo-*
759 *phys. Res. Let.*, **31** (2), L02 303, doi:10.1029/2003GL019003.

760 Pickart, R. and D. Watts, 1990: Deep western boundary current variability at Cape Hatteras. *J.*
761 *Mar. Res.*, **48**, 265–791.

762 RD Instruments, 1996: Broadband ADCP advanced principles of operation. *Field Servic Technical*
763 *Paper 001 (FST-001)*, RD Instruments, 15 pp.

764 Reeh, N., H. H. Thomsen, A. K. Higgins, and A. Weidick, 2001: Sea ice and the stability of north
765 and northeast Greenland floating glaciers. *Annals of Glaciology, Vol 33*, **33**, 474–480.

766 Rhines, P., 1970: Edge-, Bottom, and Rossby waves in a rotating stratified fluid. *Geophys. Astro-*
767 *phys. Fluid Dyn.*, **1**, 273–302.

768 Richter, M.E., W.-J. von Appen, and C. Wekerle, 2018: Does the East Greenland Current exist in
769 northern Fram Strait? *Ocean Sci.*, **14**, 1147–1165, doi:10.5194/os-14-1147-2018.

770 Schaffer, J., W.-J. van Appen, P. A. Dodd, C. Hofstede, C. Mayer, L. de Steur, and T. Kanzow,
771 2017: Warm water pathways towards Nioghalvfjærdsfjorden Glacier, Northeast Greenland. *J.*
772 *Geophys. Res.*, **122**, 4004–4020, doi:10.1002/2016JC012462.

773 Schneider, W. and G. Budéus, 1995: On the generation of the Northeast Water Polynya. *J. Geo-*
774 *phys. Res.*, **100** (C3), 4269–4286.

775 Schulze, L. M. and R. S. Pickart, 2012: Seasonal variation of upwelling in the Alaskan Beaufort
776 Sea: Impact of sea ice cover. *Journal of Geophysical Research-oceans*, **117**, C06 022, doi:
777 10.1029/2012JC007985.

- 778 Sneed, W. A. and G. S. Hamilton, 2016: Recent changes in the Norske Oer Ice Barrier, coastal
779 Northeast Greenland. *Ann. Glaciol.*, **57 (73)**, 47–55, doi:10.1017/aog.2016.21.
- 780 Steffen, K. and A. Schweiger, 1991: NASA team algorithm for sea ice concentration retrieval from
781 Defense Meteorological Satellite Program Special Sensor Microwave Imager - comparison with
782 Landsat satellite imagery. *J. Geophys. Res.*, **96 (C12)**, 21 971–21 987.
- 783 Straneo, F. and P. Heimbach, 2013: North Atlantic warming and the retreat of Greenland’s outlet
784 glaciers. *Nature*, **504 (7478)**, 36–43, doi:10.1038/nature12854.
- 785 Sutherland, D. A. and C. Cenedese, 2009: Laboratory experiments on the interaction of a buoyant
786 coastal current with a canyon: Application to the East Greenland Current. *J. Phys. Oceanogr.*,
787 **39 (5)**, 1258–1271.
- 788 Sutherland, D. A. and R. S. Pickart, 2008: The East Greenland Coastal Current: Structure, vari-
789 ability, and forcing. *Progr. Oceanogr.*, **78 (1)**, 58–77.
- 790 Sutherland, D. A., F. Straneo, and R. S. Pickart, 2014: Characteristics and dynamics of two major
791 Greenland glacial fjords. *Journal of Geophysical Research-oceans*, **119 (6)**, 3767–3791, doi:
792 10.1002/2013JC009786.
- 793 Topp, R. and M. Johnson, 1997: Winter intensification and water mass evolution from yearlong
794 current meters in the Northeast Water Polynya. *J. Mar. Sys.*, **10 (1-4)**, 157–173.
- 795 Wadhams, P., J. P. Wilkinson, and S. D. McPhail, 2006: A new view of the underside of Arctic sea
796 ice. *Geophys. Res. Let.*, **33 (4)**, L04 501.
- 797 Walters, R. and C. Heston, 1982: Tidal-period variations from time-series data using low-pass
798 digital filters. *J. Phys. Oceanogr.*, **12**, 112–115.

- 799 Washam, P., K. Nicholls, A. Münchow, and L. Padman, 2019: Summer surface melt thins Green-
800 land ice shelf by enhancing channelized basal melt. *J. Glac.*, *in press*.
- 801 Yager, P. L., D. W. R. Wallace, K. M. Johnson, W. O. Smith, P. J. Minnett, and J. W. Deming, 1995:
802 The Northeast Water Polynya as an atmospheric CO₂ sink: A seasonal rectification hypothesis.
803 *J. Geophys. Res.*, **100 (C3)**, 4389–4398, doi:10.1029/94JC01962.
- 804 Zhao, B. and M.-L. Timmermans, 2018: Topographic Rossby waves in the Arctic Ocean’s Beau-
805 fort Gyre. *J. Geophys. Res.*, **123**, 6521–6530.

806 **LIST OF TABLES**

807 **Table 1.** Mooring locations and records. Design-B moorings average 120 pings per en-
 808 semble every 30 minutes while Design-A moorings average 40 pings every 2
 809 hours. Both mooring designs have 8-m vertical bin sizes. Heading is the mag-
 810 netic compass correction from a complex (vector) correlation of tidal currents
 811 against model predictions at depth H_{model} with r^2 the fraction of the correlated
 812 variance. Mooring M70 was deployed 2014-15 as M71 to be redeployed 2015-
 813 16 as M72 with a 30 hour gap on 29/30 August 2015 between the two records.
 814 40

815 **Table 2.** Basic statistics of depth-averaged currents. Mean directions and ellipse orien-
 816 tations are in degrees positive counter-clockwise from true east. The degrees
 817 of freedom (dof) are determined as the ratio of the record length $T=792$ days
 818 and the integral decorrelation time scale T_d . Mean flows are not significantly
 819 different from zero at 95% confidence at M10 and M20 for speed. Uncertainty
 820 in directions are 95% confidence limits from directional statistics that use dof
 821 and a mean resultant length R of current vectors on a unit circle (Mardia 1972). . . . 41

822 **Table 3.** Estimated Topographic Rossby Wave properties. The wave period T is esti-
 823 mated from the frequency-domain location of kinetic energy maxima. Cross-
 824 spectra estimate phase lags at these periods that are used to estimate phase
 825 speed C_p , group velocity C_g , wave length λ , and, from the dispersion relation,
 826 the orientation ϕ_{ana} of the wave number vector relative to the upslope direction
 827 ($38T$). Positive angles are counter-clockwise. A second independent estimate
 828 of this angle is ϕ_{obs} which is derived from band-passed filtered, time-domain
 829 estimation of the ocean current ellipse orientations. Additional ellipse parame-
 830 ters are semi-major R_{maj} and minor R_{min} axes. 42

831 TABLE 1. Mooring locations and records. Design-B moorings average 120 pings per ensemble every 30
832 minutes while Design-A moorings average 40 pings every 2 hours. Both mooring designs have 8-m vertical bin
833 sizes. Heading is the magnetic compass correction from a complex (vector) correlation of tidal currents against
834 model predictions at depth H_{model} with r^2 the fraction of the correlated variance. Mooring M70 was deployed
835 2014-15 as M71 to be redeployed 2015-16 as M72 with a 30 hour gap on 29/30 August 2015 between the two
836 records.

Name	Longitude, W	Latitude, N	Depth, m	H_{model} , m	Bins	Design	Heading	r^2
M10	16.2972	77.3898	173	161	17	B	-18.6	0.753
M20	16.0458	77.4257	272	268	30	B	12.1	0.848
M30	15.7753	77.4653	303	305	32	B	33.4	0.880
M40	15.4420	77.7092	369	374	41	B	-48.0	0.890
M50	14.6478	77.9252	456	453	49	A	-0.6	0.751
M60	14.5020	77.9632	402	409	45	B	45.6	0.668
M71	14.3102	77.9975	250	347	24	A	0.0	0.772
M72	14.3102	77.9975	250	347	24	A	-11.8	0.779

837 TABLE 2. Basic statistics of depth-averaged currents. Mean directions and ellipse orientations are in degrees
838 positive counter-clockwise from true east. The degrees of freedom (dof) are determined as the ratio of the record
839 length $T=792$ days and the integral decorrelation time scale T_d . Mean flows are not significantly different from
840 zero at 95% confidence at M10 and M20 for speed. Uncertainty in directions are 95% confidence limits from
841 directional statistics that use dof and a mean resultant length R of current vectors on a unit circle (Mardia 1972).

Name	km	Mean Speed	Direction	R	Major/Minor Axis	Orientation	dof
M10	7	0.8±0.9	180±180	0.11	8.4/4.2	64	140
M20	14	1.4±1.5	-106±70	0.15	7.1/4.3	78	90
M30	22	1.8±1.5	-68±40	0.25	7.0/4.5	81	73
M40	46	0.7±0.7	-158±50	0.14	4.9/4.1	71	143
M50	76	2.4±1.1	137±20	0.35	6.9/4.1	137	157
M60	82	6.7±1.2	142±7	0.69	9.2/3.8	138	209
M70	87	4.1±1.3	156±17	0.41	9.2/4.9	131	167

842 TABLE 3. Estimated Topographic Rossby Wave properties. The wave period T is estimated from the
843 frequency-domain location of kinetic energy maxima. Cross-spectra estimate phase lags at these periods that
844 are used to estimate phase speed C_p , group velocity C_g , wave length λ , and, from the dispersion relation, the
845 orientation ϕ_{ana} of the wave number vector relative to the upslope direction ($38T$). Positive angles are counter-
846 clockwise. A second independent estimate of this angle is ϕ_{obs} which is derived from band-passed filtered,
847 time-domain estimation of the ocean current ellipse orientations. Additional ellipse parameters are semi-major
848 R_{maj} and minor R_{min} axes.

Period T	Γ^2	C_p	C_g	λ	Decay μ^{-1}	ϕ_{ana}	ϕ_{obs}	R_{maj}/R_{min}	Scale
days	-	km/day	km/day	km	m	deg.	deg.	-	days
6.5	0.73	6.8	44	93	197	175.9	175.9	6	3.5 to 7
11.2	0.76	6.0	67	140	298	177.8	177.0	8	7 to 14
19.3	0.69	3.2	63	131	280	178.7	177.5	8	14 to 28

849 **LIST OF FIGURES**

850 **Fig. 1.** Map of Northeast Greenland with 2014-16 mooring array near Isle de France across Norske
851 Trough. Red triangles place weather data from Station Nord (81.2 N), Henrik Krøyer Holme
852 (80.5° N), and Denmark Havn (76.9° N). Gray box indicates area of mooring locations (red
853 symbols) with local along-slope (308°T) and across-slope (218°T) orientation indicated by
854 black axes. Black contours indicate 250-m and 300-m depth on the continental shelf (light
855 blue) and 1000, 1100, and 1200-m water depths at the shelf break of Fram Strait (dark blue).
856 White contour indicates maximal offshore extent of landfast sea ice in 2014. Yellow symbols
857 are CTD station locations. Insert at top right shows our study area off Greenland as a red
858 dot while the insert at bottom right details locations of 7 moorings in red and 12 CTD cast
859 from 2016 in yellow. 46

860 **Fig. 2.** Sea ice cover (a), wind vectors (b), and (c) air temperatures from an automated weather
861 station at Henrik Krøyer Holme from 1st of June, 2014 through 31st of August, 2016. The
862 fractional sea ice cover (a) is from daily SSM/I imagery estimated for the small boxed area
863 shown in Figure-1. Red lines in (b) and (c) indicate variations due to a mean and annual
864 signal fitted to the data. Dashed lines in (a) indicate 15% and 85% ice cover and symbols
865 indicate time of satellite imagery of ice cover that we show in Fig. 3. 47

866 **Fig. 3.** Visible image of study area on 15 June 2014 (left panel) and 30 August 2014 (right panel)
867 from MODIS Terra. Red vectors represent the depth averaged, time-mean currents at seven
868 mooring locations (Table 2). Bottom contours (blue) and 2014 extend of landfast sea ice
869 (yellow) are the same as in Figure 1. Note the landfast ice in June to the north of our
870 mooring locations that became mobile ice in August. 48

871 **Fig. 4.** Potential temperature and salinity across Norske Trough on 9/10 June 2014 with seven 2014-
872 16 ADCP mooring deployment locations (bottom triangles) labeled M10 through M70. CTD
873 stations are small triangles at the surface. View is along the canyon towards the coast. White
874 contour lines near the bottom are in 0.1 psu and 0.1 °C for salinity and potential temperature,
875 respectively. The temperature maximum of 1.7 °C occurs at 340 m depth near km-75. Blue
876 line indicates maximal vertical stratification (stability frequency maximum) below 50-m
877 depth. 49

878 **Fig. 5.** As Figure-4, but for 15/16 Aug. 2016. The temperature maximum of 1.9 °C occurs at 290
879 m depth near km-85. 50

880 **Fig. 6.** Velocity across north-eastern slope of Norske Trough from 2014-16 ADCP moorings. View
881 is along the canyon towards the coastal glaciers. Three symbols near bottom are location
882 of bottom-mounted ADCPs at M50, M60, and M70. Red colors indicate flow into the page
883 towards the north-west (319°T). Tick marks on the right axis indicate vertical bin locations.
884 Two temperature contours are shown in yellow (0 and 1 °C) from a June 2014 CTD survey
885 shown in Fig. 4 while blue contour and symbols identify the depth of maximal stability
886 frequency to represent the pycnocline. 51

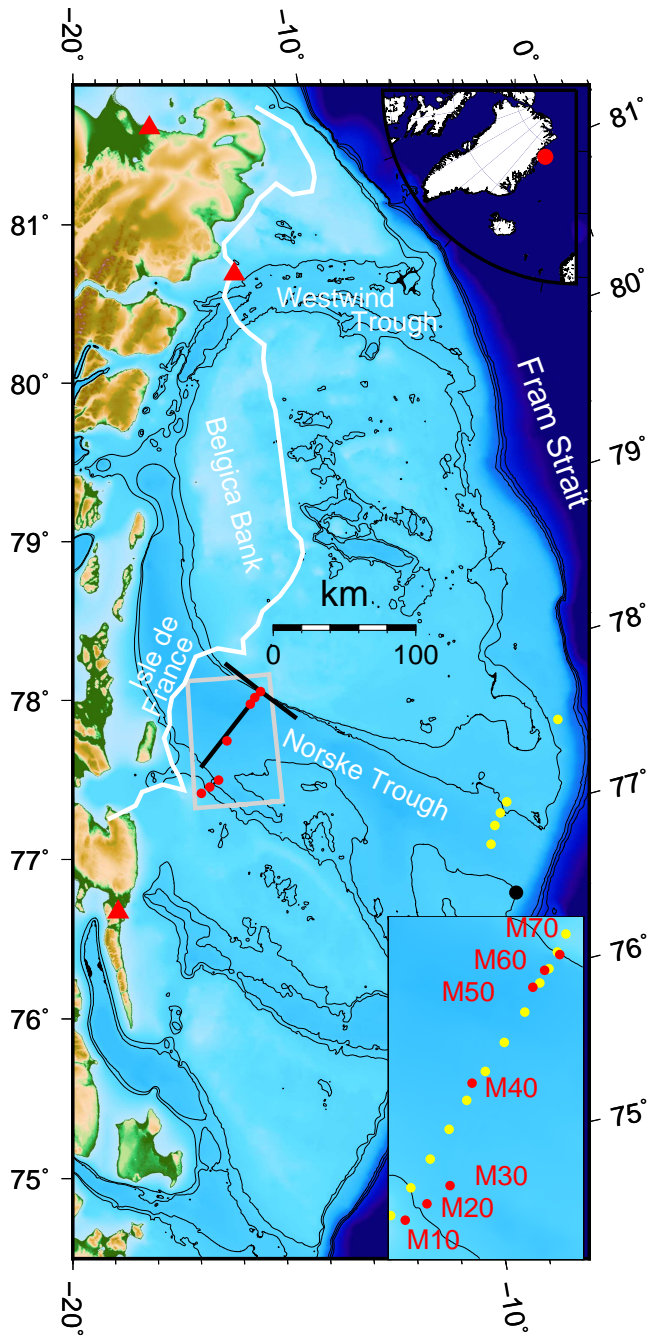
887 **Fig. 7.** Time series of ocean volume flux below 150 m depth. Flux data are band-pass filtered (19-
888 21 days) to emphasize low-frequency (Rossby wave) variability. The subtidal flux is shown
889 in light gray while the time mean flux is the horizontal line at $Q_0 = 0.27 \pm 0.06$ Sv. 52

890 **Fig. 8.** Time series of ocean current vectors at selected depths at the center of the jet (M60) over
891 the north-eastern canyon wall. Note the bottom-intensified flow. A Lanczos low-pass filter
892 removes variability at time scales smaller than 5 days to emphasize mean and low-frequency
893 variability. 53

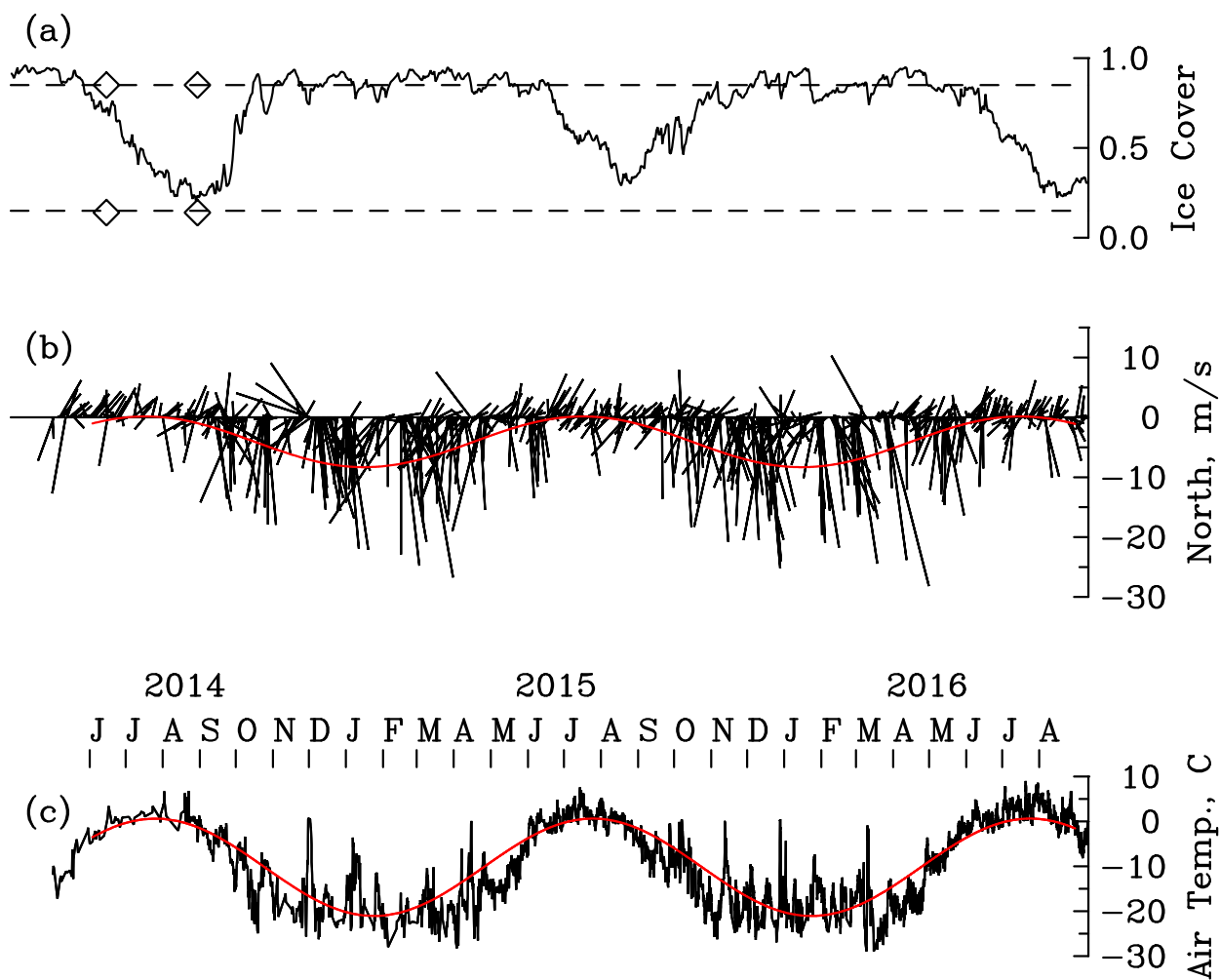
894	Fig. 9.	Velocity components along (black symbols) and across (red line) Norske Trough at M60 (319°T) with 95% uncertainty of speed and direction. Temperature profiles at the location are shown in the right panel from June 2014 in red and August 2016 in black.	54
897	Fig. 10.	Temporal and vertical variability at the center of the inflowing jet (M60) organized by empirical orthogonal analysis. Time series are in unitless standard deviations while vertical patterns have units of cm/s. The variance explained by each mode is listed. Red lines fit an annual cycle to the time series.	55
901	Fig. 11.	Distribution of variance with frequency for the EOF-1 (solid line) and EOF-2 (dotted line) shown in Figs. 10a and b, respectively.	56
903	Fig. 12.	Coherence (bottom) and phase (top) of along-canyon flows at M60 (303-m) and M50 (309-m) with frequency. Positive phase indicates correlated signals appear first at BG60 to propagate offshore to M50. Coherence estimates above 0.15 are significantly different from zero at 95% confidence.	57
907	Fig. 13.	Ocean current ellipses (red) at 231m, 215m, and 237m at mooring locations M50, M60, and M70, respectively. Along-slope (x) and across-slope (y) co-ordinate axes are shown (gray) along with a scale for ellipses (black). Group and phase velocity vectors are shown in blue for a topographic Rossby wave with a period of 19.3 days (Table 3).	58
911	Fig. 14.	Surface wind vectors on 17 December, 2015 with Ekman pumping velocities (color) estimated from the curl of the wind-stress (ERA-interim). Bottom topography at 250, 1000, 1100, and 1200 m is indicated by blue contours, red triangles show ocean mooring locations while black circles indicate locations of Ekman pumping velocity time series shown in Figs. 16 and 17.	59
916	Fig. 15.	Coherence Γ^2 between 786-day long time series of Ekman pumping velocities and near-bottom currents along the slope of Norske Trough in the [19,21] day frequency band. Bottom topography at 250, 1000, 1100, and 1200 m is indicated by blue contours, black triangles show locations of ocean moorings. Black contours highlight the topographic Rossby wave source region with Γ^2 of 0.36, 0.42, 0.48; arrow indicates direction of wave group velocity; and red dots show location of reference time series shown in Fig. 17.	60
922	Fig. 16.	Power spectral density of vertical Ekman pumping velocity W_e near the shelf break at 8°W and 76.5°N latitude (top panel) and coherence with along-slope currents (bottom panel). Phase between w_e and bottom currents at 351 m depth at BG60 is shown in red only at frequencies with non-zero coherences at 99% confidence; positive phase indicates that a positive (upwelling) $w_e > 0$ leads a negative (landward) flow $u < 0$. See Figs. 13 and 17 for co-ordinate system and time domain representation of the 20-day signals.	61
928	Fig. 17.	Time series of band-pass filtered (14-28 days) Ekman pumping velocities at the 2 locations shown in Fig. 14 in black compared against similarly band-pass filtered near-bottom along-slope velocity in red. Top panel shows Ekman pumping at [15W, 78N] near the mooring location while the bottom panel shows Ekman pumping at [8W, 76.5N] near Fram Strait upstream from the mooring location.	62
933	Fig. 18.	Potential temperature vs. salinity from selected stations along the postulated path of the bottom-intensified and topographically steered flow near the 350-m isobath. Northern Fram Strait data in blue originate from Section-10 of Håvik et al. (2017) while data from eastern Norske Trough in red originate from section NT1 of Richter et al. (2018). Black symbols	

937 are data from our mooring section; for locations see Fig. 1. Contours are density anomalies,
938 thick line is freezing point temperature. 63

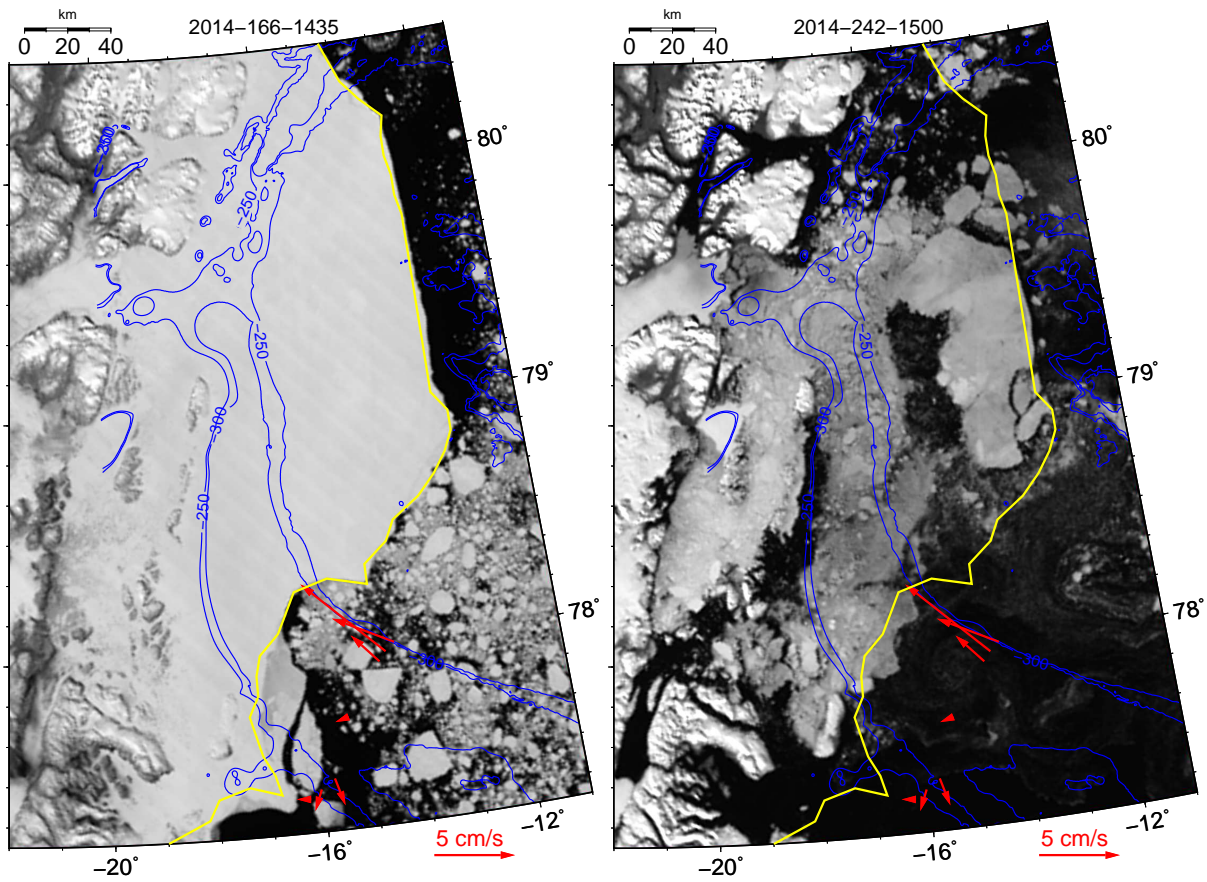
939 **Fig. A1.** Time series of pressure (top), heading (middle), and tilt angles (bottom) at M20. The mag-
940 netic compass heading shows both a steady decline of compass declination (red lines) as
941 well as spikes caused by five identified solar storms (red symbols). 64



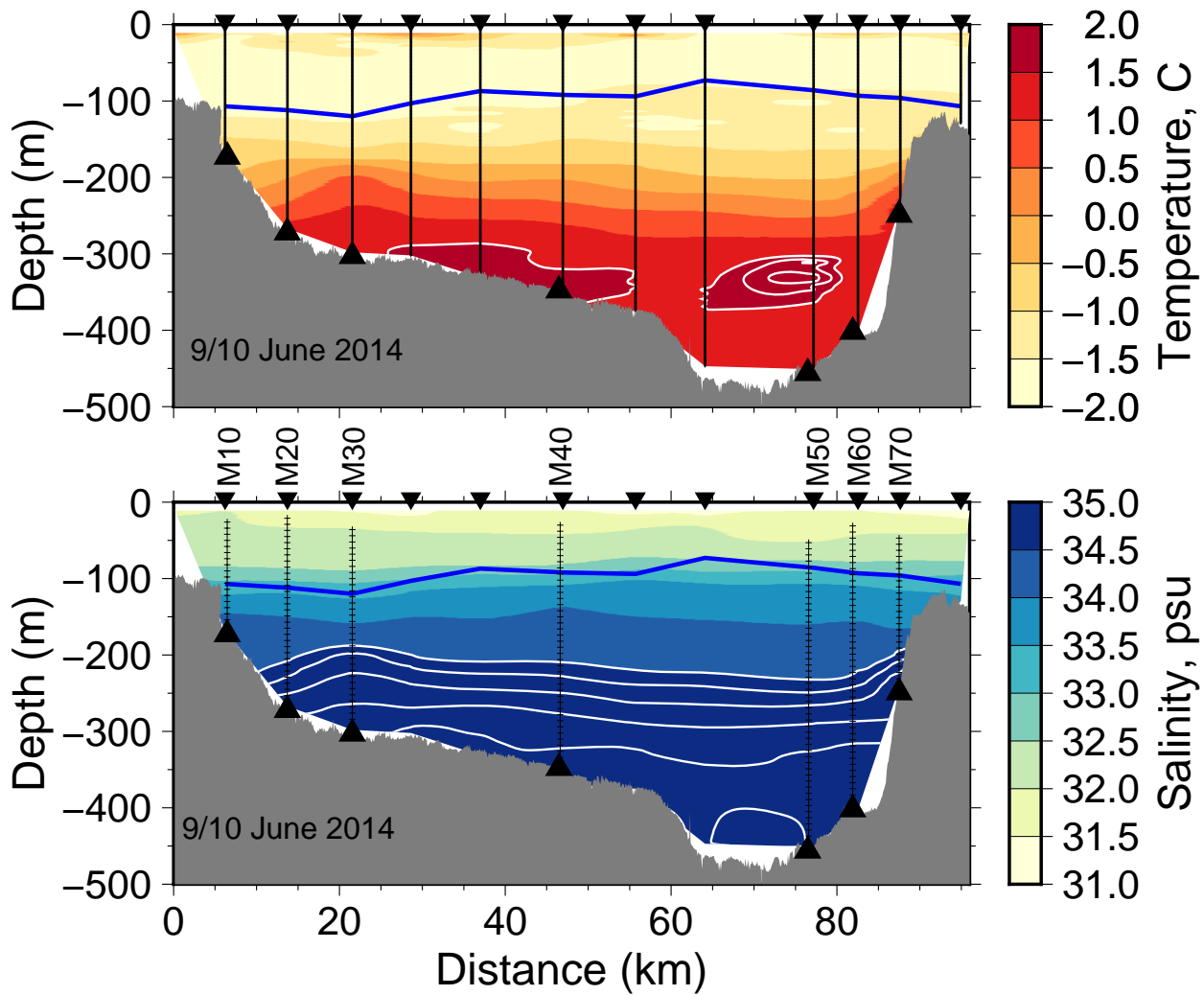
942 FIG. 1. Map of Northeast Greenland with 2014-16 mooring array near Isle de France across Norske Trough.
 943 Red triangles place weather data from Station Nord (81.2° N), Henrik Krøyer Holme (80.5° N), and Denmark
 944 Havn (76.9° N). Gray box indicates area of mooring locations (red symbols) with local along-slope (308°T) and
 945 across-slope (218°T) orientation indicated by black axes. Black contours indicate 250-m and 300-m depth on
 946 the continental shelf (light blue) and 1000, 1100, and 1200-m water depths at the shelf break of Fram Strait (dark
 947 blue). White contour indicates maximal offshore extent of landfast sea ice in 2014. Yellow symbols are CTD
 948 station locations. Insert at top right shows our study area off Greenland as a red dot while the insert at bottom
 949 right details locations of 7 moorings in red and 12 CTD cast from 2016 in yellow.



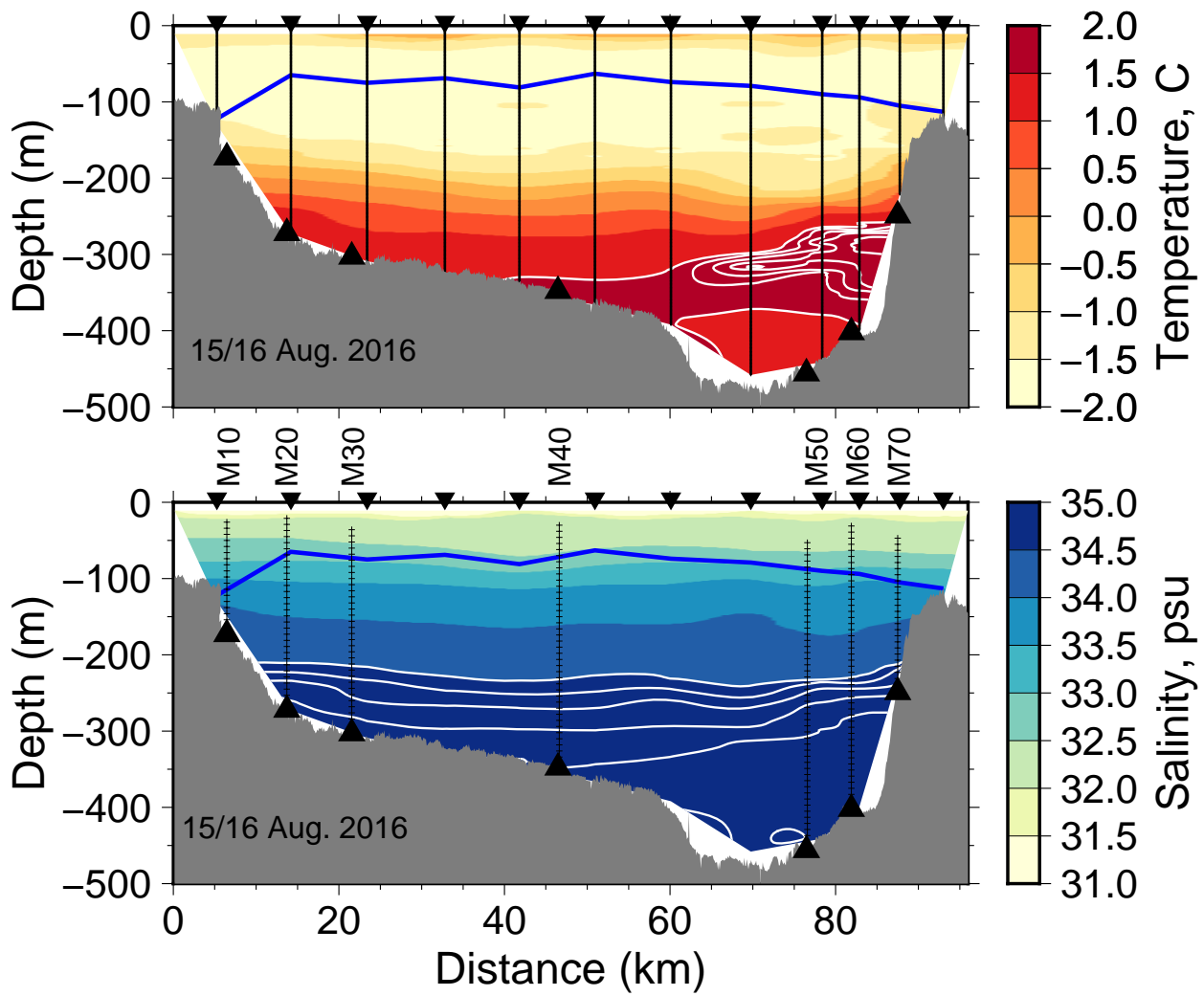
950 FIG. 2. Sea ice cover (a), wind vectors (b), and (c) air temperatures from an automated weather station at
 951 Henrik Krøyer Holme from 1st of June, 2014 through 31st of August, 2016. The fractional sea ice cover (a)
 952 is from daily SSM/I imagery estimated for the small boxed area shown in Figure-1. Red lines in (b) and (c)
 953 indicate variations due to a mean and annual signal fitted to the data. Dashed lines in (a) indicate 15% and 85%
 954 ice cover and symbols indicate time of satellite imagery of ice cover that we show in Fig. 3.



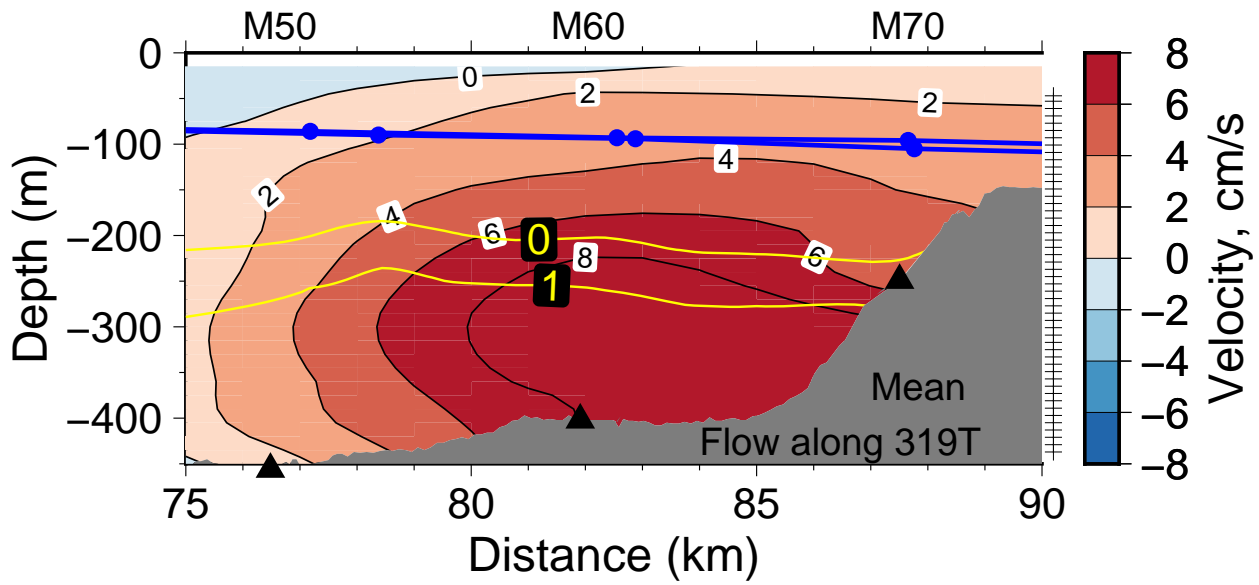
955 FIG. 3. Visible image of study area on 15 June 2014 (left panel) and 30 August 2014 (right panel) from
 956 MODIS Terra. Red vectors represent the depth averaged, time-mean currents at seven mooring locations (Table
 957 2). Bottom contours (blue) and 2014 extend of landfast sea ice (yellow) are the same as in Figure 1. Note the
 958 landfast ice in June to the north of our mooring locations that became mobile ice in August.



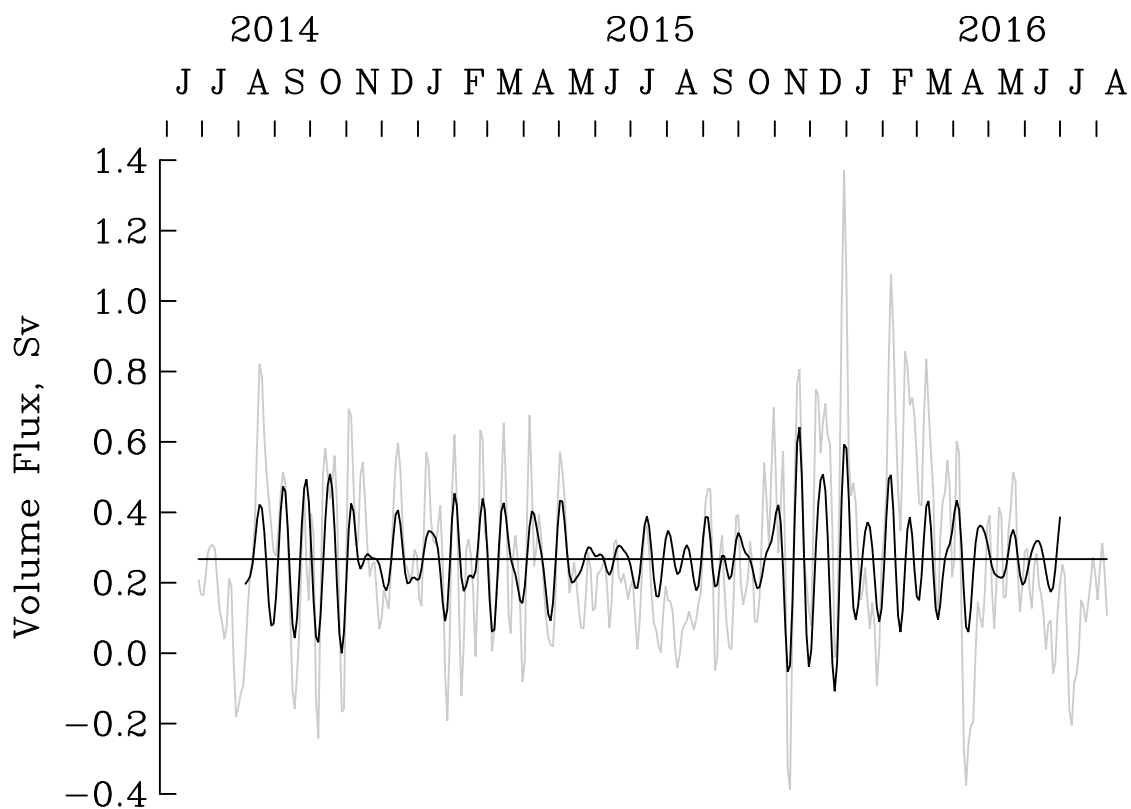
959 FIG. 4. Potential temperature and salinity across Norske Trough on 9/10 June 2014 with seven 2014-16 ADCP
 960 mooring deployment locations (bottom triangles) labeled M10 through M70. CTD stations are small triangles at
 961 the surface. View is along the canyon towards the coast. White contour lines near the bottom are in 0.1 psu and
 962 0.1 °C for salinity and potential temperature, respectively. The temperature maximum of 1.7 °C occurs at 340
 963 m depth near km-75. Blue line indicates maximal vertical stratification (stability frequency maximum) below
 964 50-m depth.



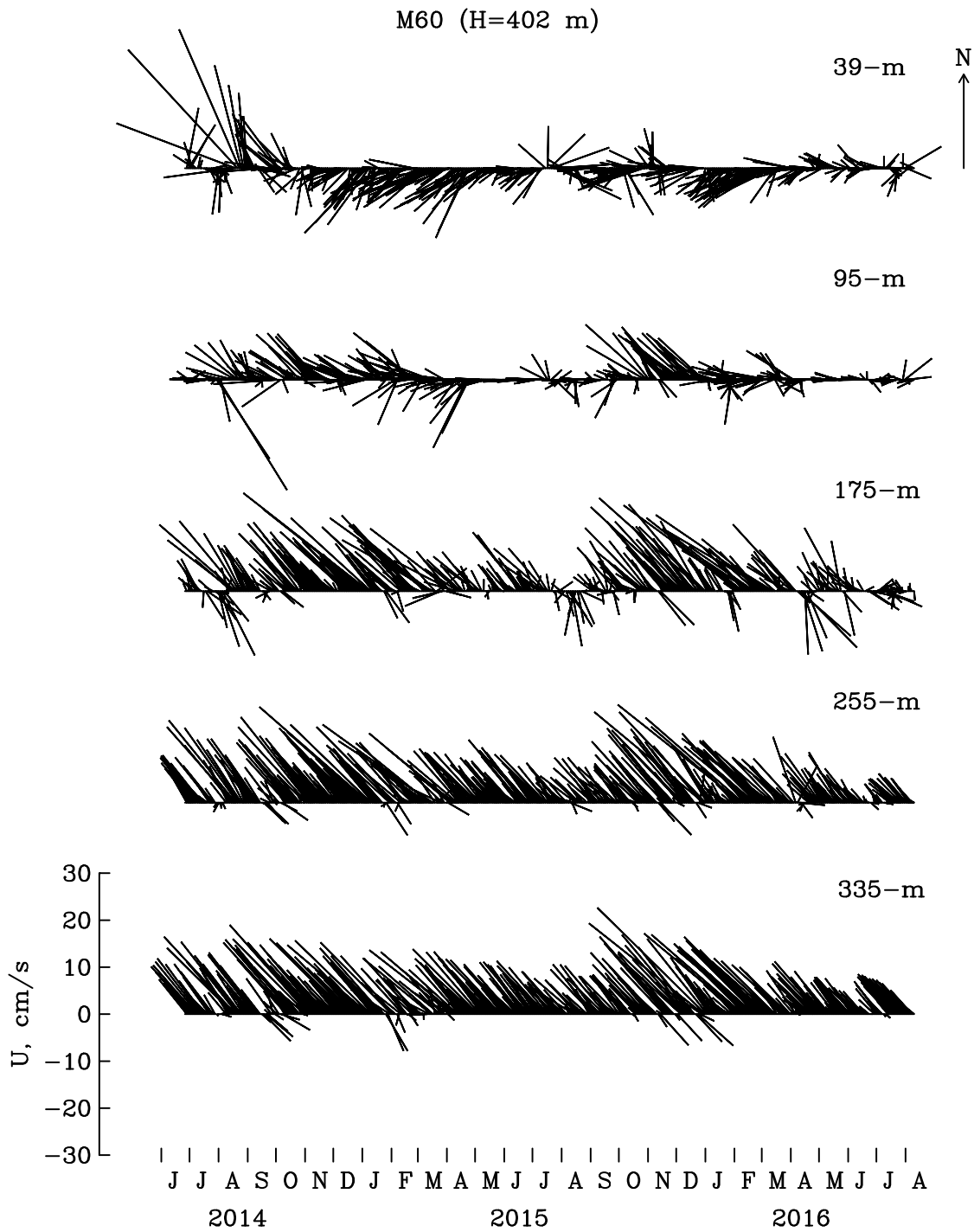
965 FIG. 5. As Figure-4, but for 15/16 Aug. 2016. The temperature maximum of 1.9 °C occurs at 290 m depth
 966 near km-85.



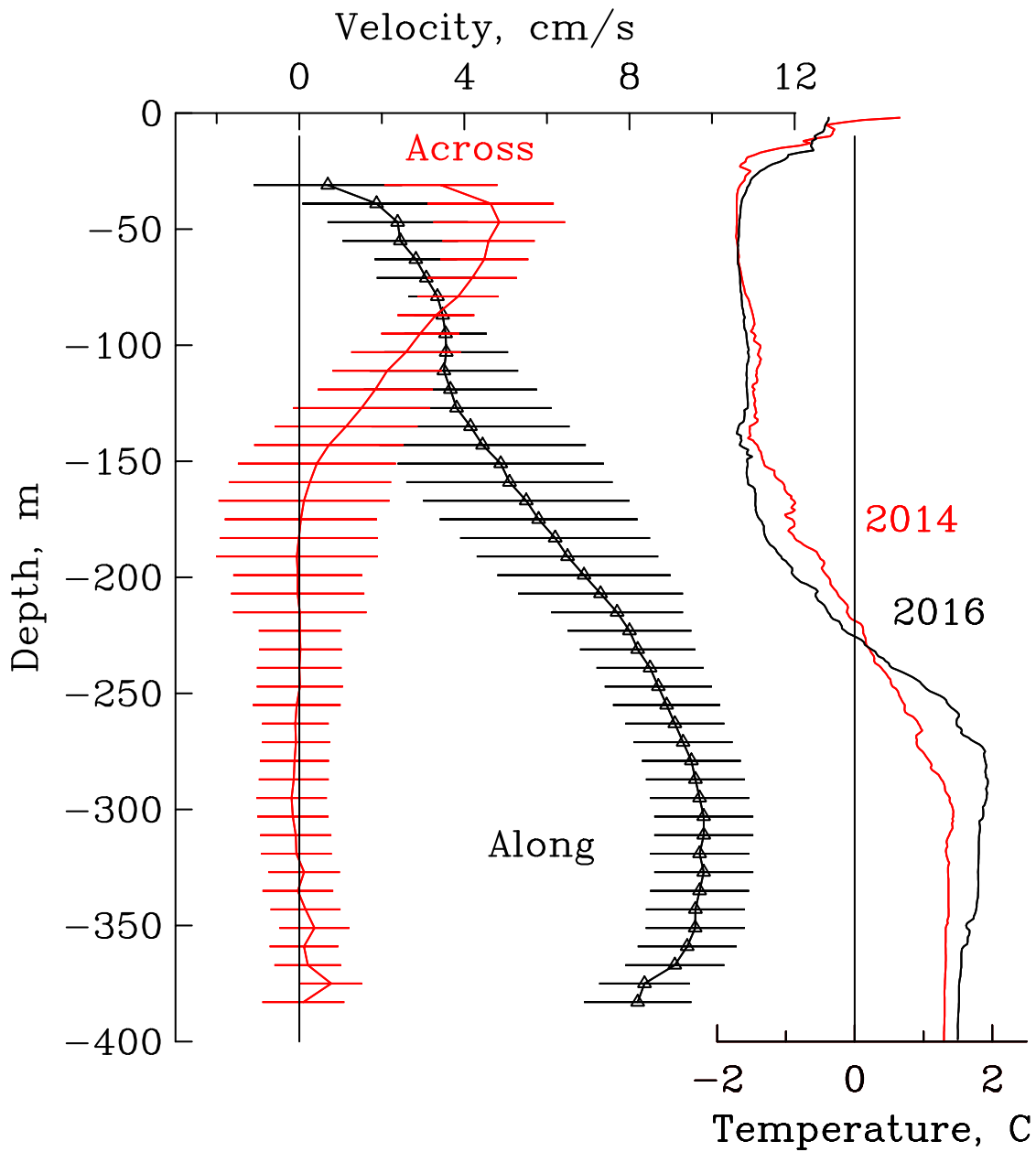
967 FIG. 6. Velocity across north-eastern slope of Norske Trough from 2014-16 ADCP moorings. View is along
 968 the canyon towards the coastal glaciers. Three symbols near bottom are location of bottom-mounted ADCPs at
 969 M50, M60, and M70. Red colors indicate flow into the page towards the north-west (319°T). Tick marks on the
 970 right axis indicate vertical bin locations. Two temperature contours are shown in yellow (0 and 1 °C) from a
 971 June 2014 CTD survey shown in Fig. 4 while blue contour and symbols identify the depth of maximal stability
 972 frequency to represent the pycnocline.



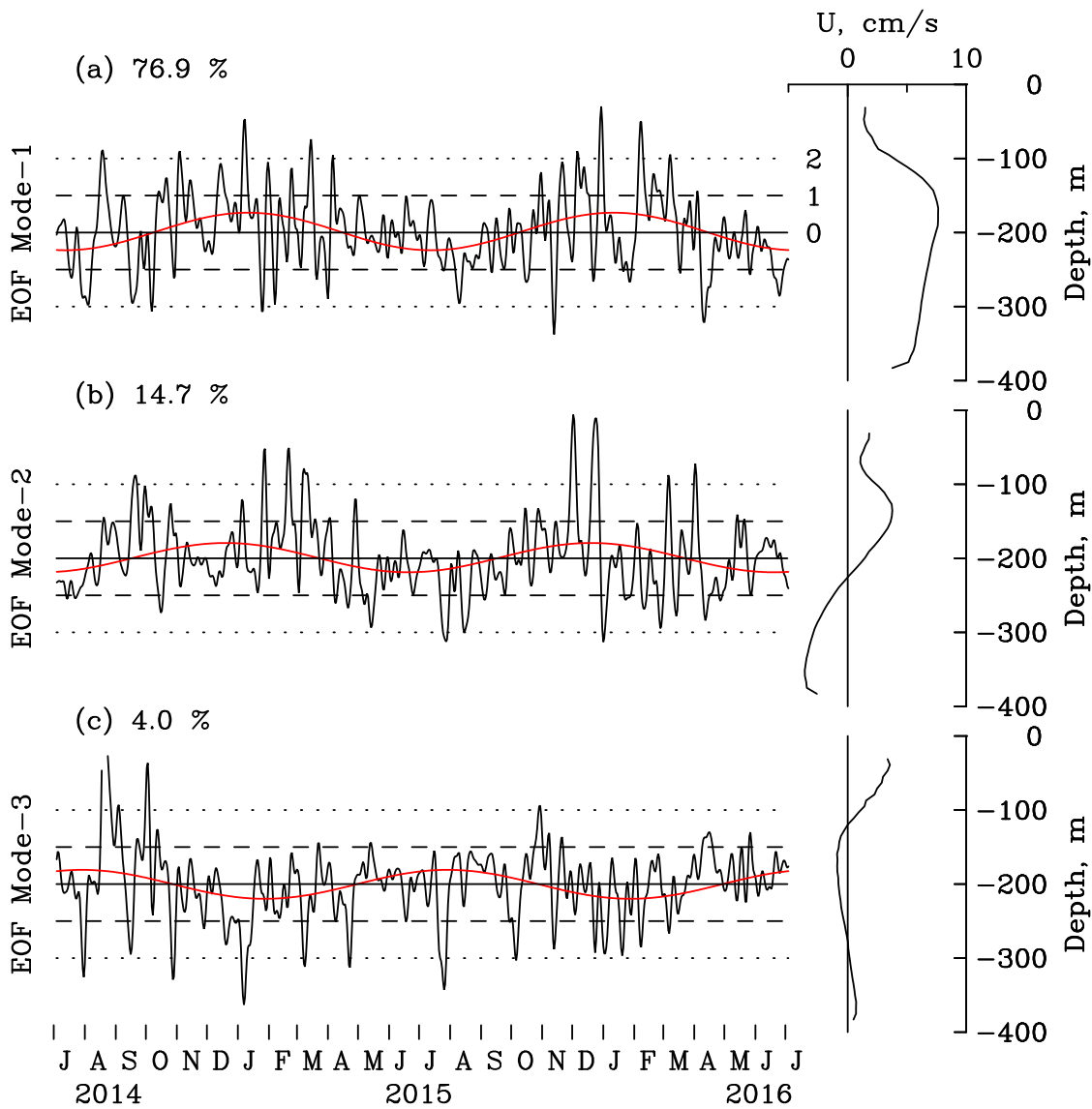
973 FIG. 7. Time series of ocean volume flux below 150 m depth. Flux data are band-pass filtered (19-21 days)
 974 to emphasize low-frequency (Rossby wave) variability. The subtidal flux is shown in light gray while the time
 975 mean flux is the horizontal line at $Q_0 = 0.27 \pm 0.06$ Sv.



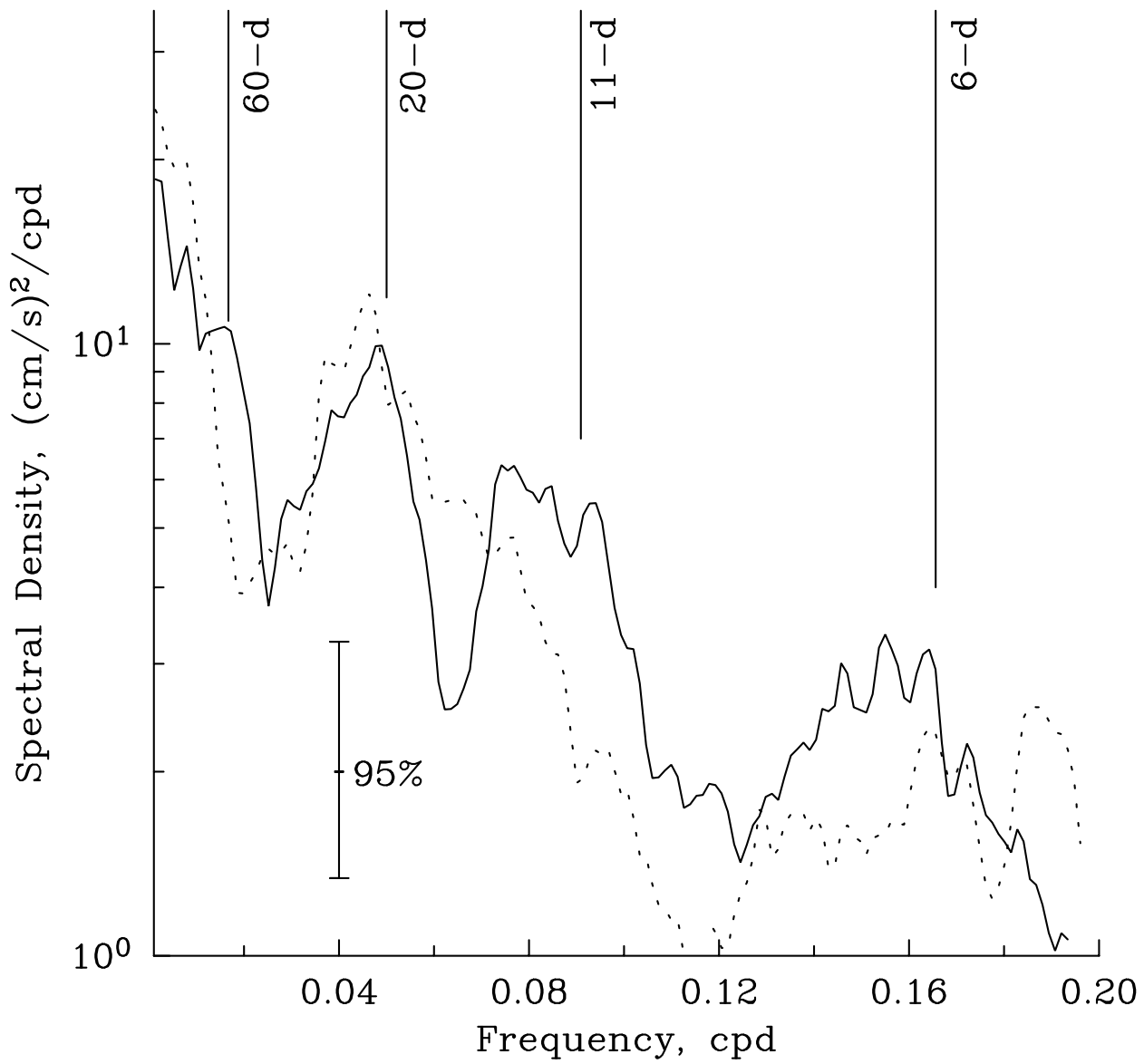
976 FIG. 8. Time series of ocean current vectors at selected depths at the center of the jet (M60) over the north-
 977 eastern canyon wall. Note the bottom-intensified flow. A Lanczos low-pass filter removes variability at time
 978 scales smaller than 5 days to emphasize mean and low-frequency variability.



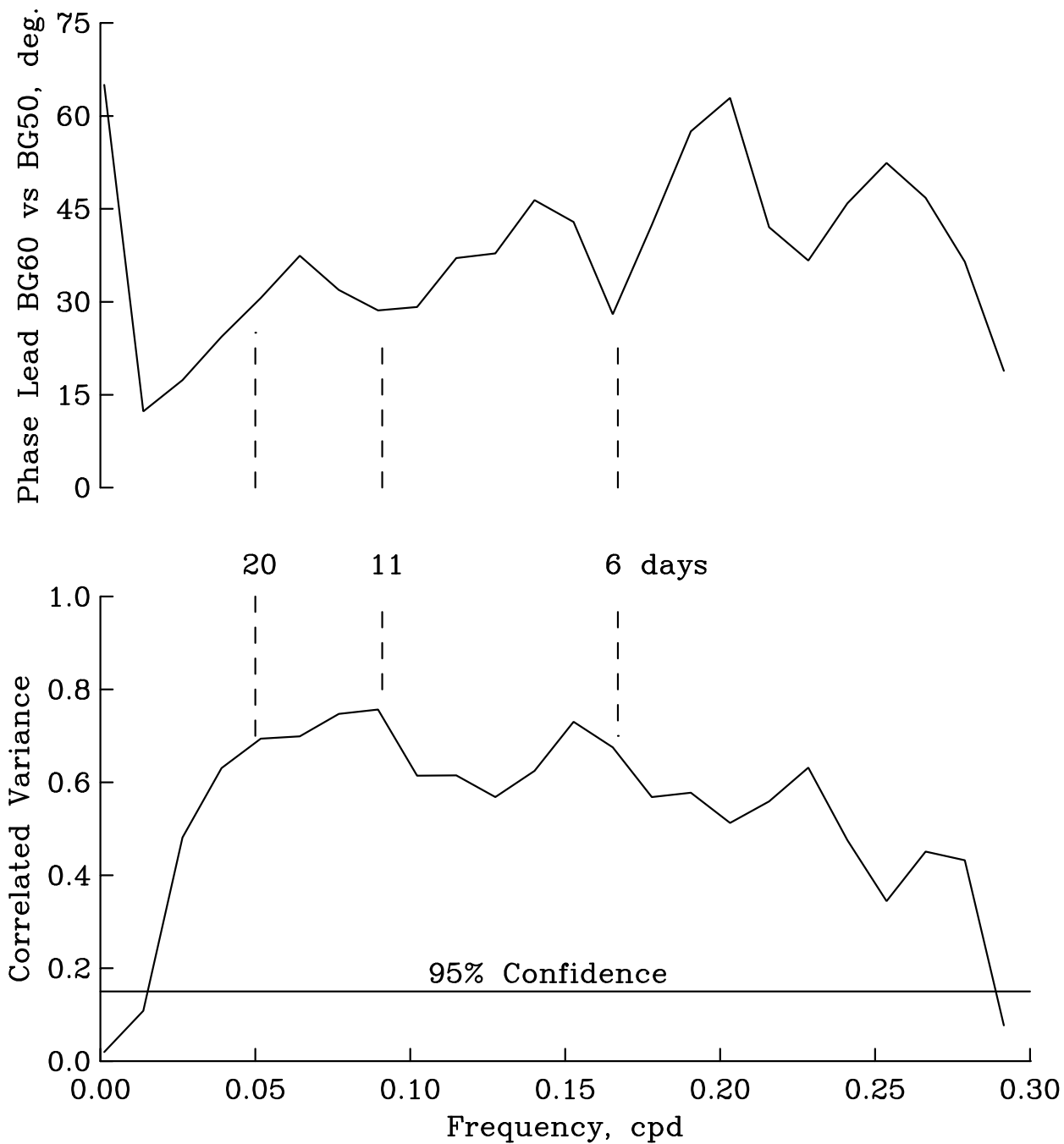
979 FIG. 9. Velocity components along (black symbols) and across (red line) Norske Trough at M60 (319°T) with
 980 95% uncertainty of speed and direction. Temperature profiles at the location are shown in the right panel from
 981 June 2014 in red and August 2016 in black.



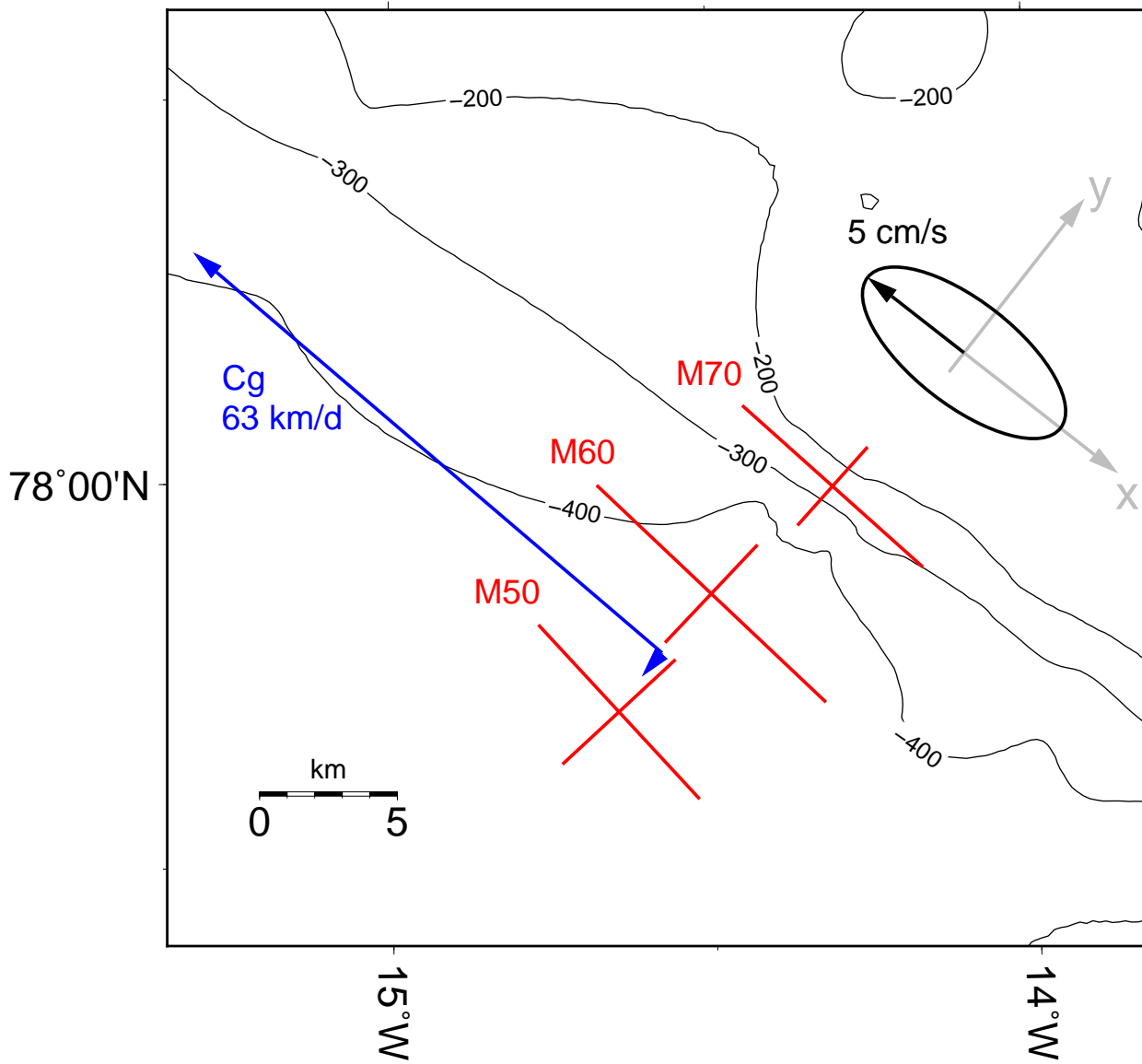
982 FIG. 10. Temporal and vertical variability at the center of the inflowing jet (M60) organized by empirical
 983 orthogonal analysis. Time series are in unitless standard deviations while vertical patterns have units of cm/s.
 984 The variance explained by each mode is listed. Red lines fit an annual cycle to the time series.



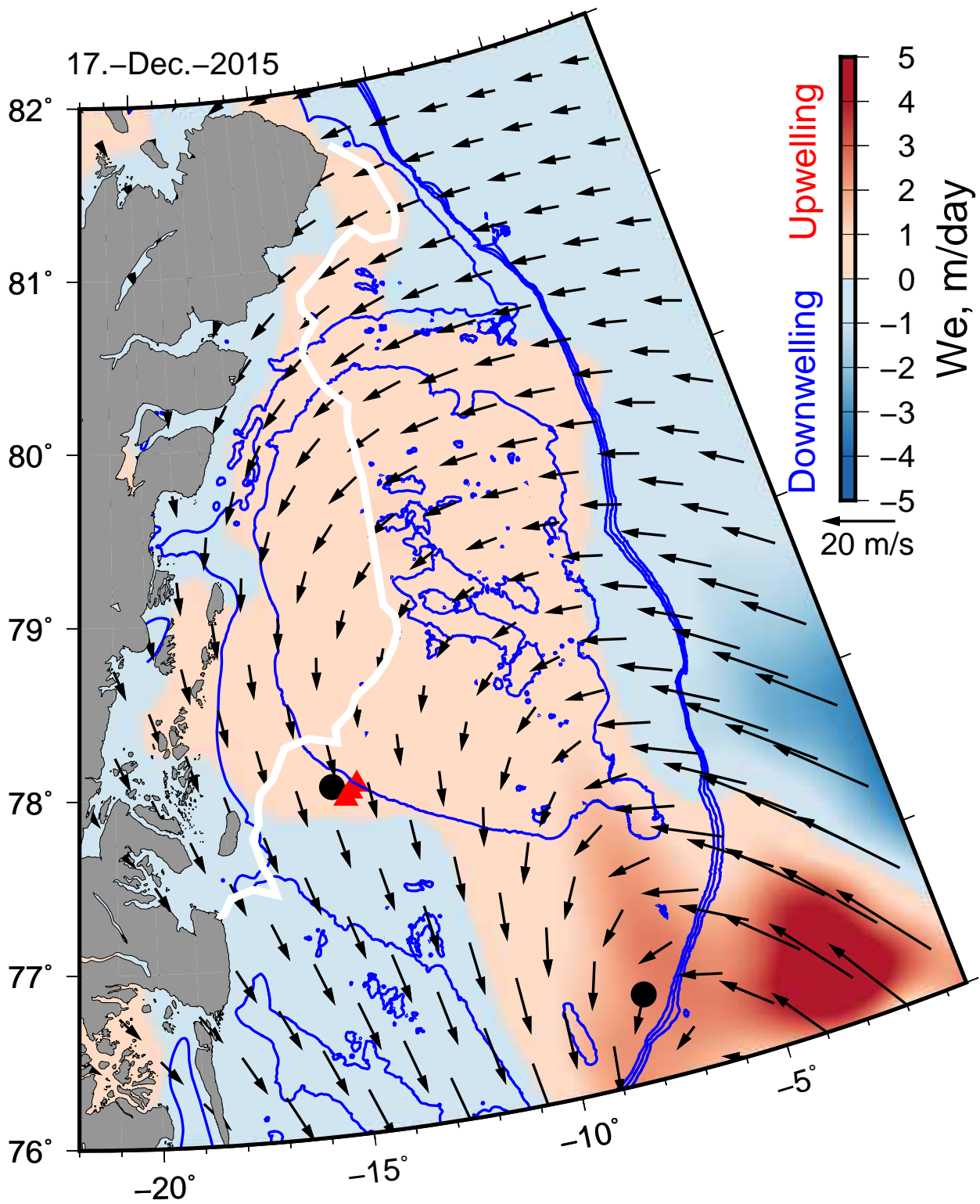
985 FIG. 11. Distribution of variance with frequency for the EOF-1 (solid line) and EOF-2 (dotted line) shown in
 986 Figs. 10a and b, respectively.



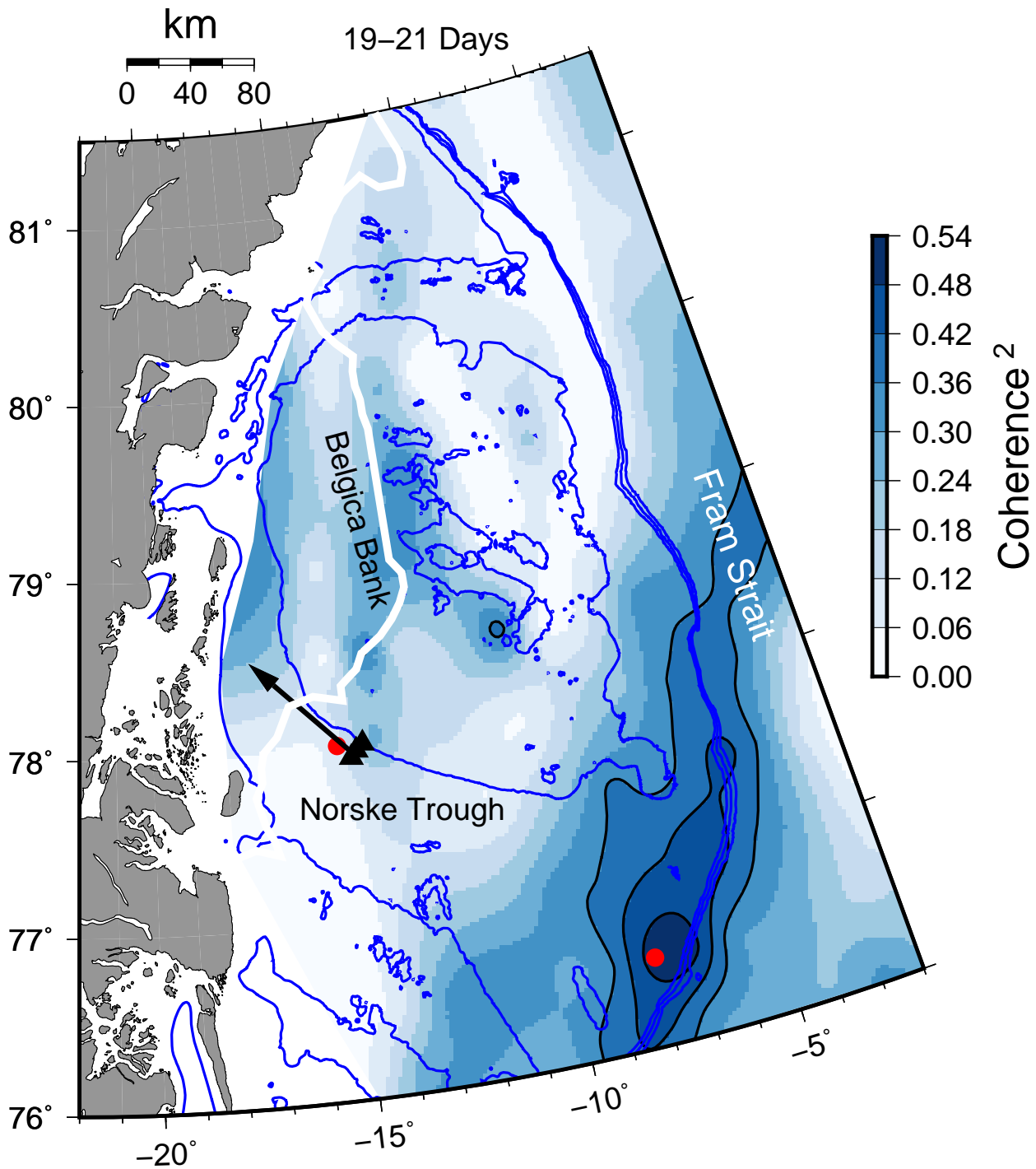
987 FIG. 12. Coherence (bottom) and phase (top) of along-canyon flows at M60 (303-m) and M50 (309-m)
 988 with frequency. Positive phase indicates correlated signals appear first at BG60 to propagate offshore to M50.
 989 Coherence estimates above 0.15 are significantly different from zero at 95% confidence.



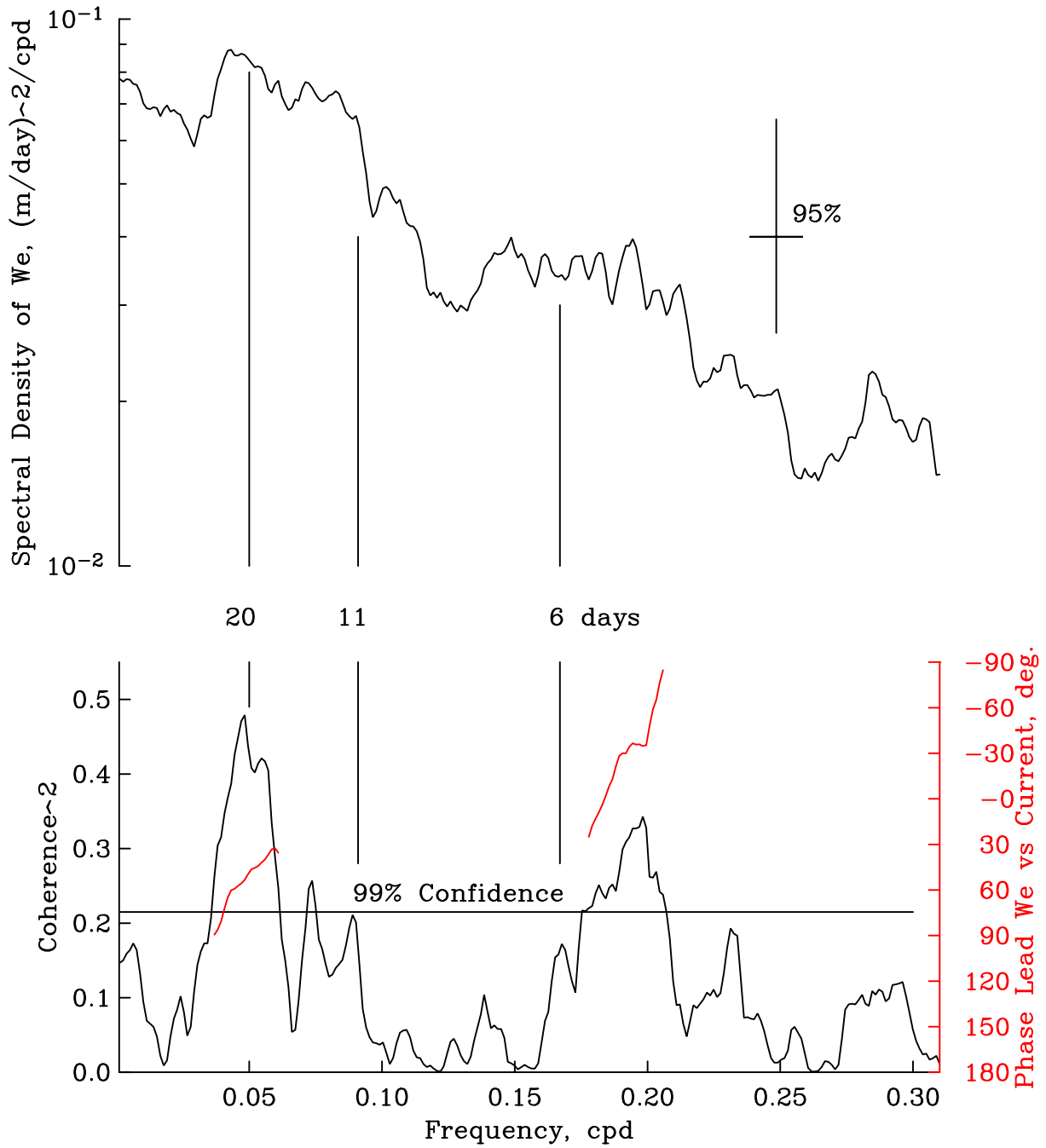
990 FIG. 13. Ocean current ellipses (red) at 231m, 215m, and 237m at mooring locations M50, M60,
 991 respectively. Along-slope (x) and across-slope (y) co-ordinate axes are shown (gray) along with a scale for
 992 ellipses (black). Group and phase velocity vectors are shown in blue for a topographic Rossby wave with a
 993 period of 19.3 days (Table 3).



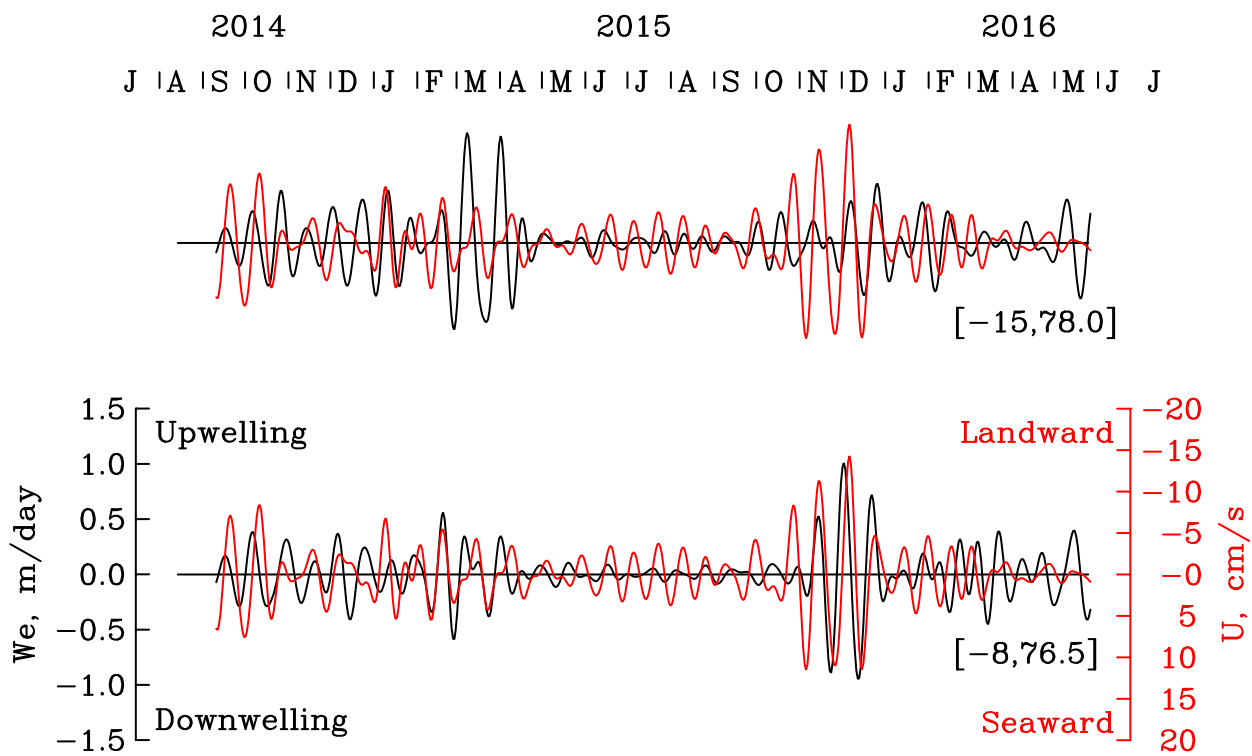
994 FIG. 14. Surface wind vectors on 17 December, 2015 with Ekman pumping velocities (color) estimated from
 995 the curl of the wind-stress (ERA-interim). Bottom topography at 250, 1000, 1100, and 1200 m is indicated
 996 by blue contours, red triangles show ocean mooring locations while black circles indicate locations of Ekman
 997 pumping velocity time series shown in Figs. 16 and 17.⁵⁹



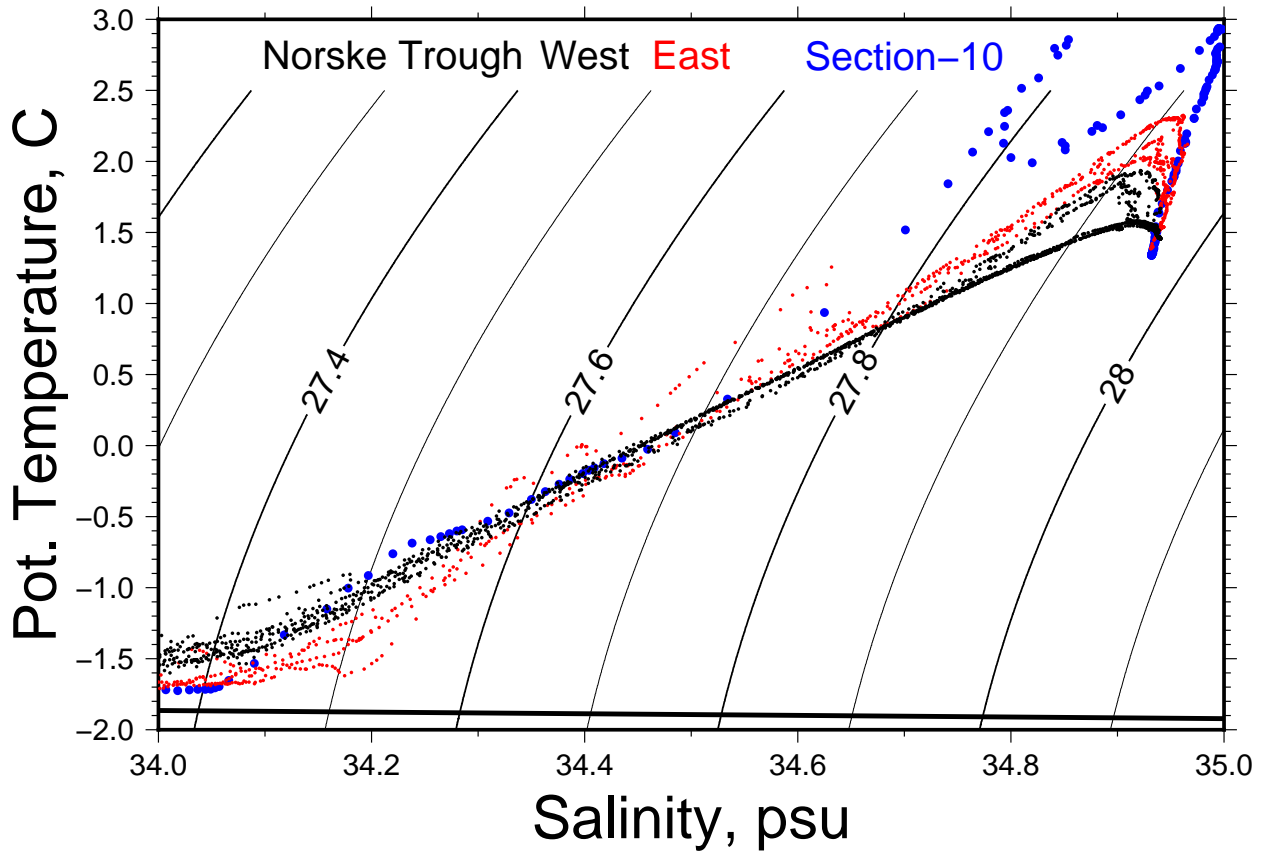
998 FIG. 15. Coherence Γ^2 between 786-day long time series of Ekman pumping velocities and near-bottom
 999 currents along the slope of Norske Trough in the [19,21] day frequency band. Bottom topography at 250, 1000,
 1000 1100, and 1200 m is indicated by blue contours, black triangles show locations of ocean moorings. Black
 1001 contours highlight the topographic Rossby wave source region with Γ^2 of 0.36, 0.42, 0.48; arrow indicates
 1002 direction of wave group velocity; and red dots show location of reference time series shown in Fig. 17.



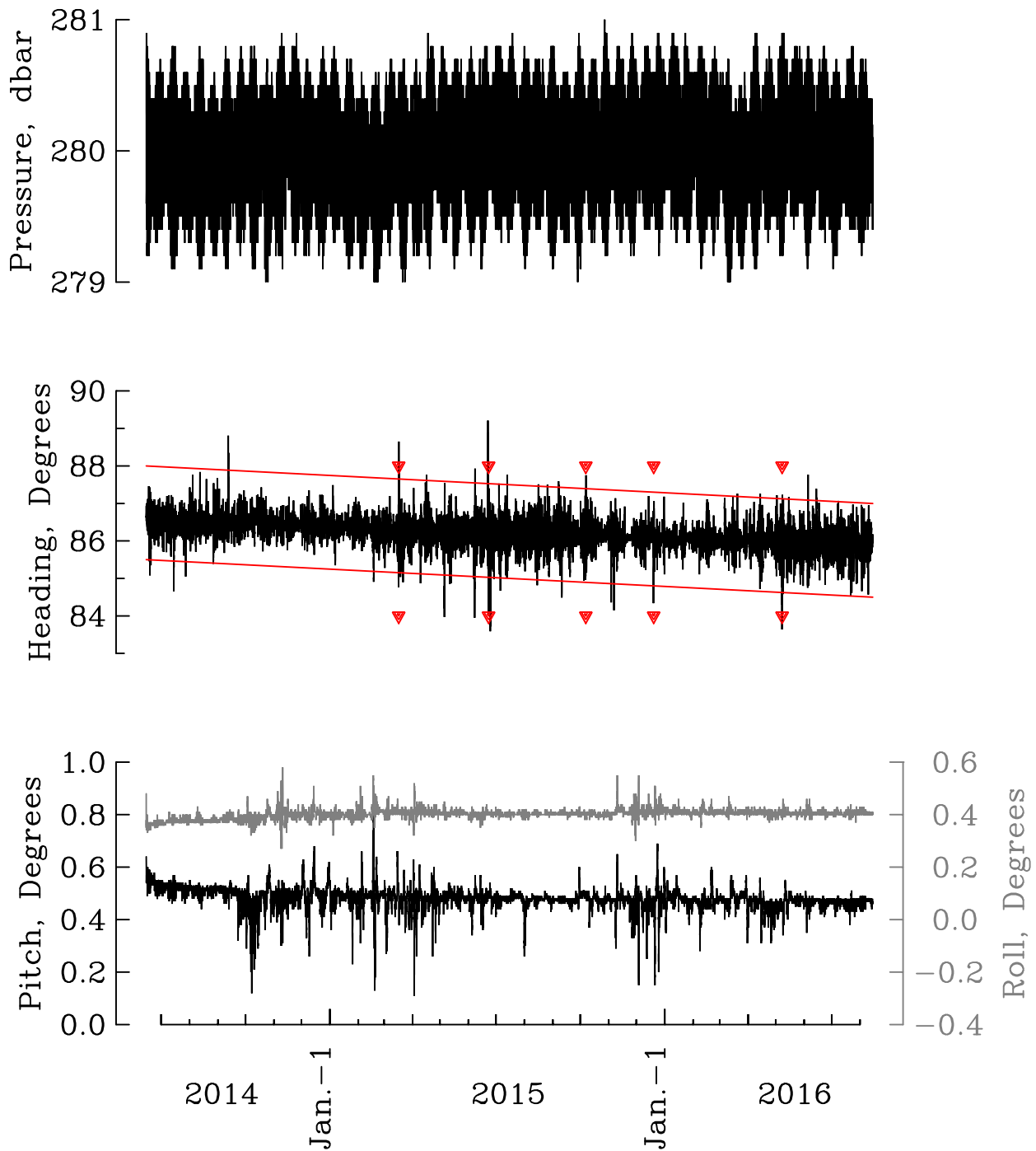
1003 FIG. 16. Power spectral density of vertical Ekman pumping velocity W_e near the shelf break at 8°W and
 1004 76.5°N latitude (top panel) and coherence with along-slope currents (bottom panel). Phase between w_e and
 1005 bottom currents at 351 m depth at BG60 is shown in red only at frequencies with non-zero coherences at 99%
 1006 confidence; positive phase indicates that a positive (upwelling) $w_e > 0$ leads a negative (landward) flow $u < 0$.
 1007 See Figs. 13 and 17 for co-ordinate system and time domain representation of the 20-day signals.



1008 FIG. 17. Time series of band-pass filtered (14-28 days) Ekman pumping velocities at the 2 locations shown
 1009 in Fig. 14 in black compared against similarly band-pass filtered near-bottom along-slope velocity in red. Top
 1010 panel shows Ekman pumping at [15W, 78N] near the mooring location while the bottom panel shows Ekman
 1011 pumping at [8W, 76.5N] near Fram Strait upstream from the mooring location.



1012 FIG. 18. Potential temperature vs. salinity from selected stations along the postulated path of the bottom-
 1013 intensified and topographically steered flow near the 350-m isobath. Northern Fram Strait data in blue originate
 1014 from Section-10 of Håvik et al. (2017) while data from eastern Norske Trough in red originate from section NT1
 1015 of Richter et al. (2018). Black symbols are data from our mooring section; for locations see Fig. 1. Contours
 1016 are density anomalies, thick line is freezing point temperature.



1017 Fig. A1. Time series of pressure (top), heading (middle), and tilt angles (bottom) at M20. The magnetic
 1018 compass heading shows both a steady decline of compass declination (red lines) as well as spikes caused by five
 1019 identified solar storms (red symbols).